










# 53BP1 loss elicits cGAS-STING-dependent antitumor immunity in ovarian and pancreatic cancer

Received: 15 March 2024

Accepted: 29 July 2024

Published online: 06 August 2024

 Check for updates

Yajie Sun <sup>1,2,9</sup>, Jeffrey Patterson-Fortin<sup>1,3,9</sup>, Sen Han<sup>4</sup>, Zhe Li <sup>4</sup>,  
Zuzanna Nowicka <sup>5</sup>, Yuna Hirohashi<sup>1,6</sup>, Susan Kilgas <sup>1</sup>, Jae Kyo Yi<sup>1</sup>,  
Alexander Spektor <sup>1,7</sup>, Wojciech Fendler <sup>5,6</sup>,  
Panagiotis A. Konstantinopoulos <sup>3</sup> & Dipanjan Chowdhury <sup>1,7,8</sup> 

53BP1 nucleates the anti-end resection machinery at DNA double-strand breaks, thereby countering BRCA1 activity. Loss of 53BP1 leads to DNA end processing and homologous recombination in BRCA1-deficient cells. Consequently, BRCA1-mutant tumors, typically sensitive to PARP inhibitors (PARPi), become resistant in the absence of 53BP1. Here, we demonstrate that the ‘leaky’ DNA end resection in the absence of 53BP1 results in increased micronuclei and cytoplasmic double-stranded DNA, leading to activation of the cGAS-STING pathway and pro-inflammatory signaling. This enhances CD8<sup>+</sup> T cell infiltration, activates macrophages and natural killer cells, and impedes tumor growth. Loss of 53BP1 correlates with a response to immune checkpoint blockade (ICB) and improved overall survival. Immunohistochemical assessment of 53BP1 in two malignancies, high grade serous ovarian cancer and pancreatic ductal adenocarcinoma, which are refractory to ICBs, reveals that lower 53BP1 levels correlate with an increased adaptive and innate immune response. Finally, BRCA1-deficient tumors that develop resistance to PARPi due to the loss of 53BP1 are susceptible to ICB. Therefore, we conclude that 53BP1 is critical for tumor immunogenicity and underpins the response to ICB. Our results support including 53BP1 expression as an exploratory biomarker in ICB trials for malignancies typically refractory to immunotherapy.

Maintenance of genome integrity is of utmost importance for cellular survival<sup>1</sup>. Genome integrity is achieved by DNA repair pathways, collectively known as the DNA damage response (DDR)<sup>2</sup>. Double-stranded breaks (DSBs) are the most cytotoxic form of DNA damage and, if unrepaired, these lesions lead to deleterious outcomes such as

permanent changes to DNA sequence, cellular death, or cancer<sup>1–6</sup>. The majority of DSBs are rapidly repaired by the non-homologous end-joining (NHEJ) pathway, in which DSB DNA ends are directly re-ligated with minimal processing. NHEJ is an error prone and template independent DSB repair pathway that occurs throughout the entire cell

<sup>1</sup>Division of Radiation and Genome Stability, Department of Radiation Oncology, Dana-Farber Cancer Institute, Harvard Medical School, Boston, MA, USA.

<sup>2</sup>Cancer Center, Union Hospital, Tongji Medical College, Huazhong University of Science and Technology, Wuhan, PR China. <sup>3</sup>Department of Medical Oncology, Dana-Farber Cancer Institute, Harvard Medical School, Boston, MA, USA. <sup>4</sup>Division of Genetics, Brigham and Women’s Hospital, Harvard Medical School, Boston, MA, USA. <sup>5</sup>Department of Biostatistics and Translational Medicine, Medical University of Lodz, Lodz, Poland. <sup>6</sup>Center for DNA Damage and Repair, Dana-Farber Cancer Institute, Harvard Medical School, Boston, MA, USA. <sup>7</sup>Broad Institute of Harvard and MIT, Cambridge, MA, USA. <sup>8</sup>Department of Biological Chemistry & Molecular Pharmacology, Harvard Medical School, Boston, MA, USA. <sup>9</sup>These authors contributed equally: Yajie Sun, Jeffrey Patterson-Fortin. ✉ e-mail: [dipanjan\\_chowdhury@dfci.harvard.edu](mailto:dipanjan_chowdhury@dfci.harvard.edu)

cycle, though mainly in G1. During S and G2 phases of the cell cycle, DSB repair can occur by homologous recombination (HR), mediated by BRCA1 and BRCA2 which is sequence-guided by the available sister chromatid. The first step of HR is the generation of 3' overhanging single-stranded (ssDNA) by end resection. The choice between NHEJ and HR is regulated by 53BP1 by preventing the early step of DNA end-resection at DSBs<sup>7–9</sup> and at deprotected telomeres<sup>10–12</sup>. When DSBs occur, 53BP1 is rapidly recruited to DNA lesions and serves as the cornerstone of the anti-resection machinery. 53BP1 constitutively binds DYNLL1 and brings it to DSBs thereby blocking MRE11-mediated end resection<sup>13–15</sup>. In response to DNA damage, ATM-mediated phosphorylation of 53BP1 recruits the Shieldin complex and factors RIF1 and PTIP to DNA damage sites further impeding DNA end resection<sup>16–22</sup>. Although the molecular role of 53BP1 in maintaining genome stability in dividing cells is well-studied, there is limited understanding of how 53BP1 influences tumor homeostasis and the microenvironment.

Though defects in the DDR can lead to genomic instability, contributing to the development of cancer, it also leads to a greater reliance on the remaining DDR pathways, which can be exploited by the concept of synthetic lethality<sup>23</sup>. An early example of successful exploitation of synthetic lethality was the use of poly(ADP-ribose) polymerase (PARP) inhibitors (PARPi) in the treatment of *BRCA1*- or *BRCA2*-deficient tumors defective in HR<sup>24,25</sup>. The anti-tumor synthetic lethality mediated by PARPi in *BRCA1*- or *BRCA2*-deficient tumors is multifactorial including inhibition of PARylation<sup>26</sup>, PARP trapping<sup>27</sup>, replication fork collapse<sup>28</sup>, accumulation of replication gaps<sup>29,30</sup>, and generation of cytosolic DNA which can activate the cGAS-STING leading to activation of the adaptive immune system<sup>31,32</sup>. Despite the success of PARPi, multiple mechanisms of PARPi resistance have emerged and novel strategies to overcome resistance are required<sup>23</sup>. The most studied PARPi resistance mechanism involves restoration of HR activity via *BRCA1/2* reversion<sup>33</sup> or for *BRCA1* mutant tumors via suppression of genes involved in inhibiting DNA end-resection, notably *TP53BP1*<sup>9,16,19,34–39</sup>.

Here, we show that loss of 53BP1 leads to pro-inflammatory signaling, CD8<sup>+</sup> T cell infiltration and activation of the innate immune response in high grade serous ovarian cancer (HGSOC) and pancreatic ductal adenocarcinoma (PDAC). Consistent with its molecular function, 53BP1 loss induces micronuclei and cytosolic dsDNA and activates the cGAS-STING pathway to stimulate the inflammatory response. Furthermore, loss of 53BP1 correlates with enhanced response to immune checkpoint blockade (ICB) and improved overall survival in HGSOC and PDAC, both tumor types that are typically refractory ICBs. Finally, *BRCA1*-deficient cancers that get resistant to PARPi due to loss of 53BP1, are responsive to the combination of PARPi and ICB.

## Results

### 53BP1 loss promotes T cell infiltration and is associated with improved overall survival

53BP1 is a key regulator of the DDR, required for DNA repair and tumor suppression<sup>40,41</sup>. To assess the clinical relevance of 53BP1, we evaluated *TP53BP1* expression in cohorts of patients with HGSOC and PDAC from the TCGA Pan-Cancer Atlas Studies' RNA-sequencing (RNA-seq) expression data, two clinically relevant groups of patients where PARPi therapy is FDA approved<sup>42,43</sup>. RNA-seq analysis revealed a range of *TP53BP1* expression in these tumors. Of the 201 HGSOC cases analyzed, 122 (60.7%) demonstrated low *TP53BP1* expression, 51 (25.3%) demonstrated normal expression, and the remaining 28 (14.0%) expressed *TP53BP1* at high levels, corresponding to a mRNA expression z-score less than or equal to -0.3 or greater than or equal to 0.3, respectively (Fig. 1a). Similarly, of the 167 PDAC cases analyzed, 52 (31.0%) demonstrated low *TP53BP1* expression, 75 (45.0%) demonstrated normal expression, and the remaining 40 (24.0%) expressed

*TP53BP1* at high levels (Fig. 1b). These observations revealed that *TP53BP1* expression is heterogeneous in HGSOC and PDAC.

Does 53BP1 impact anti-tumor immunity? We hypothesized that decreased *TP53BP1* expression would promote increased DNA end-resection and the production of neoantigens, a key determinant of anti-tumor immunity<sup>36,44</sup>. To test this hypothesis, we first confirmed that depletion of *TP53BP1* resulted in a significant increase in ssDNA levels (Supplementary Fig. 1a–c). Next, we analyzed tumor mutational burden (TMB) from the TCGA in correlation with *TP53BP1* expression in HGSOC and PDAC. Consistently, low *TP53BP1* expression correlated with increased TMB in both HGSOC and PDAC (Fig. 1c, d) suggesting that increased TMB or neoantigens secondary to *TP53BP1* loss could underlie decreased tumorigenesis and increased anti-tumor immunity<sup>45,46</sup>. Third, given cytotoxic CD8<sup>+</sup> T-cells are the most powerful effectors in the anti-tumor immune response<sup>47</sup>, we interrogated the TISIDB (an integrated repository portal for tumor-immune system interactions)<sup>48</sup> for the relationship between activated CD8<sup>+</sup> T-cells and *TP53BP1* expression in both HGSOC and PDAC. Decreased *TP53BP1* expression correlated with increased activated CD8<sup>+</sup> T-cell infiltration (Supplementary Fig. 1d). As 53BP1 carries out its role in regulating DNA end-resection by acting as a platform for recruitment of downstream factors (53BP1-RIF-Shieldin complex)<sup>9,16,19,37,38,49–54</sup>, we asked if decreased expression of any of these factors would similarly correlate with increased activated CD8<sup>+</sup> T-cell infiltration. Interestingly, activated CD8<sup>+</sup> T-cell infiltration correlated with different directionality for Shieldin and REV7, with decreased infiltration upon decreased expression of these factors. For decreased RIF1, PTIP and RNF168 there was increased T cell infiltration but to a lesser degree compared to decreased *TP53BP1* expression (Fig. 1e, f; Supplementary Fig. 1d). Despite its key role in DNA repair and tumor suppression, a low level of *TP53BP1* expression correlated with an improved prognosis in HGSOC (Fig. 1g)<sup>40,41,55</sup>, reinforcing the importance of 53BP1 in DNA damaging cancer therapy.

To gain insight into the mechanisms underlying how 53BP1 loss mediated immune infiltration, *Trp53bp1* was knocked out using CRISPR/Cas9 in ID8 cells, a widely used *BRCA*-proficient mouse model of ovarian cancer (Supplementary Fig. 1e, f)<sup>56</sup>. Similarly, *Trp53bp1* was knocked out in a murine PDAC cell line derived from late-stage primary tumors from an autochthonous mouse model of *Kras*<sup>G12D</sup> and *Trp53*<sup>R172H</sup>-mutated PDAC (KPC) (Supplementary Fig. 1e, g)<sup>57</sup>. Subcutaneous injection of wildtype or *Trp53bp1* knockout (KO) HGSOC or PDAC cells into immune competent syngeneic animals resulted in allograft tumors, creating a tractable system to study 53BP1 loss in vivo (Supplementary Fig. 1e). Next, we conducted RNA-sequencing (RNA-seq) analysis of wildtype and *Trp53bp1* KO PDAC and HGSOC tumors. To understand changes in biological pathways and systems upon *Trp53bp1* loss, we performed Kyoto Encyclopedia of Genes and Genomes (KEGG) analysis (Fig. 1h; Supplementary Fig. 1h)<sup>58</sup>. Additionally, we employed Gene Set Enrichment Analysis to query the differentially expressed genes against the "Hallmark" database (Fig. 1i; Supplementary Fig. 1i). Consistent with the hypothesis that 53BP1 loss correlates with anti-tumor immune response via increased TMB, both pathway analyses demonstrated a robust enrichment in cytokine signaling and inflammatory pathways, and concomitant upregulation of inflammatory gene expression (Supplementary Fig. 1j).

### 53BP1 depletion inhibits tumor growth by activating inflammatory signaling

We next interrogated the hypothesis that 53BP1 loss inhibits tumor growth by inducing an extrinsic immune-mediated anti-tumor response as in vitro, parental or *Trp53bp1* KO cells exhibited similar proliferation rates (Supplementary Fig. 2a, b) and similar activation of apoptosis (Supplementary Fig. 2c, d), arguing against an intrinsic etiology. To assess the possible link between 53BP1 expression and tumor growth inhibition, we employed two mouse PDAC tumor engraftment models (subcutaneous and orthotopic) and one mouse HGSOC tumor

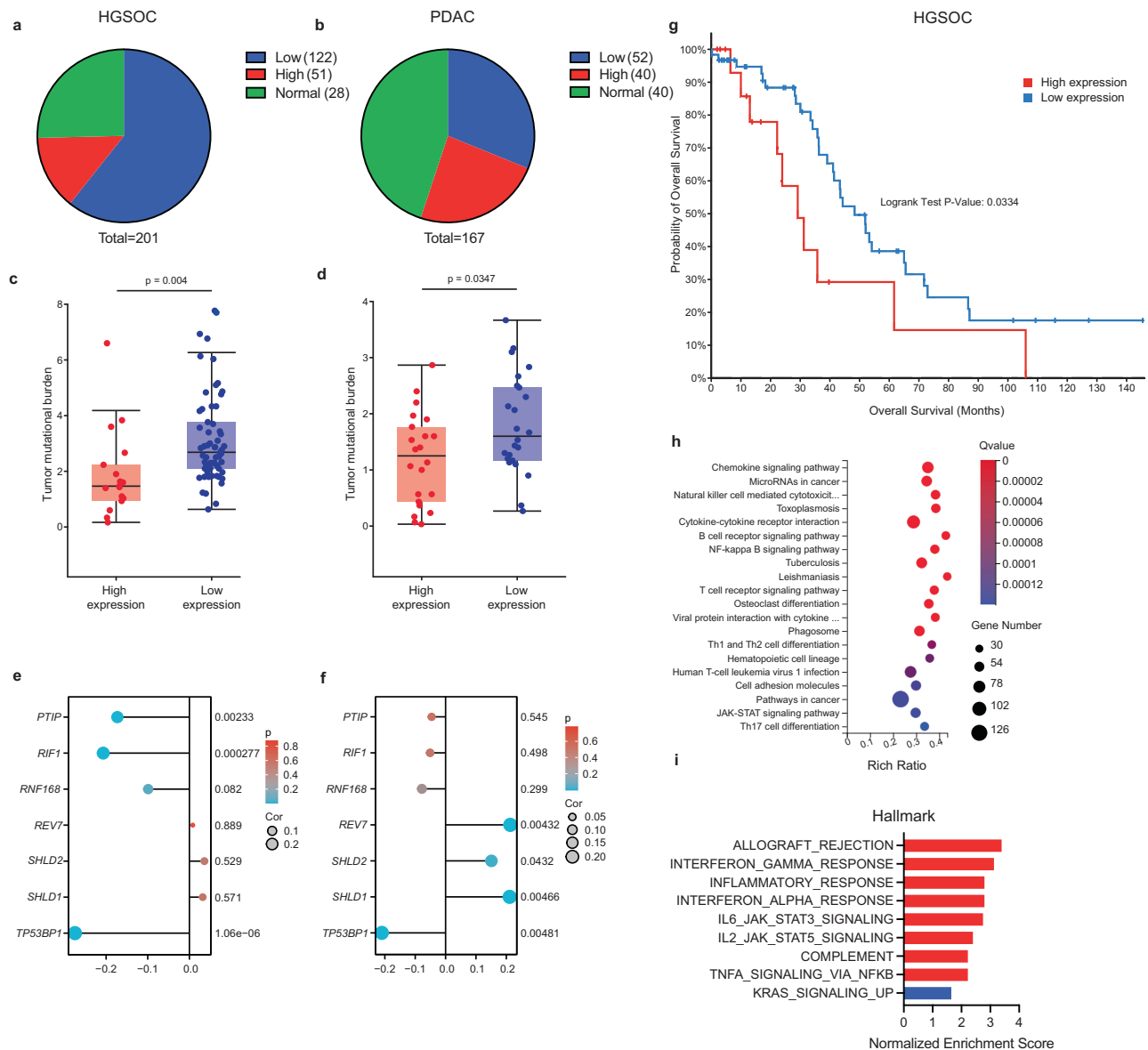


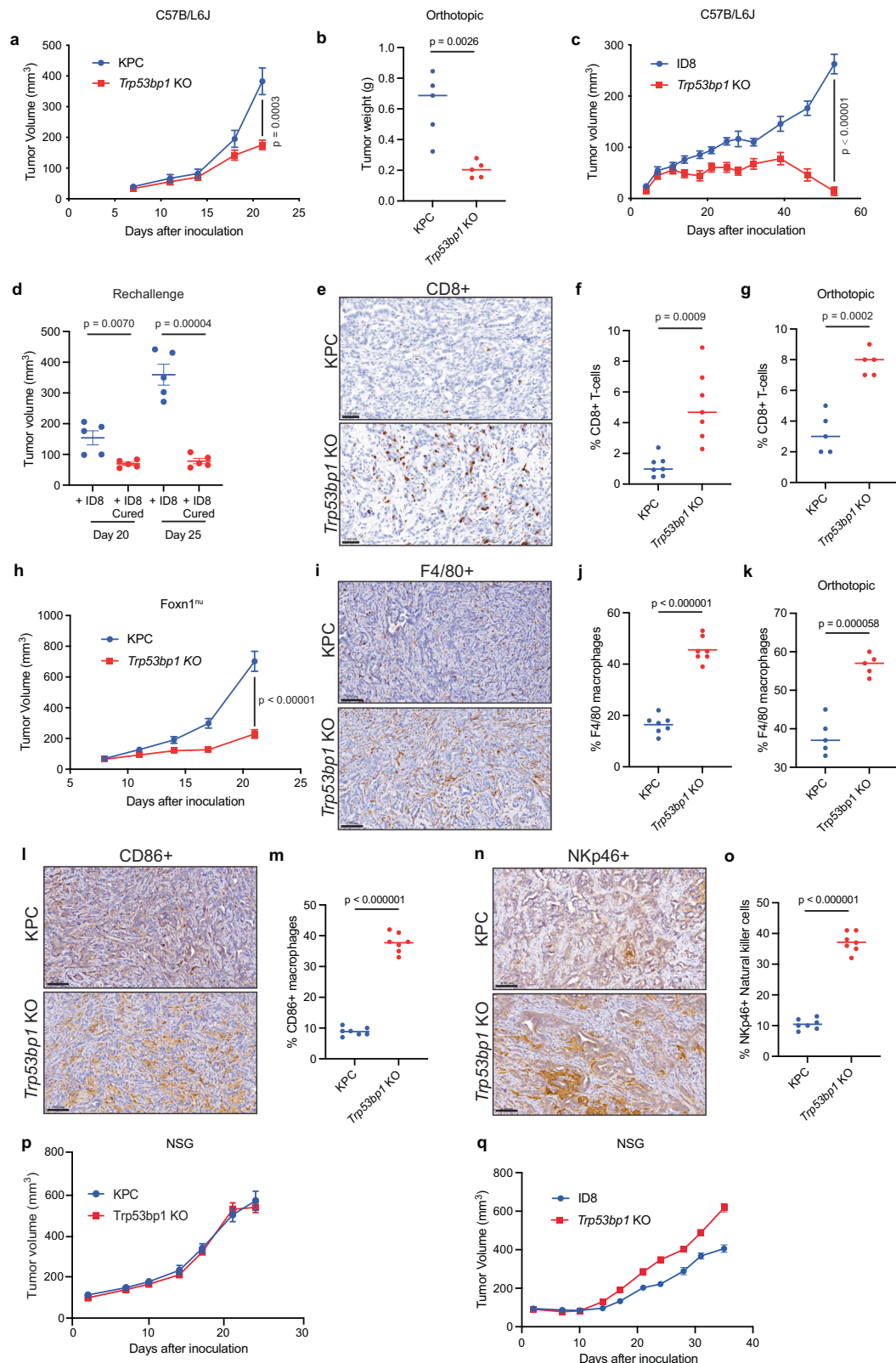
**Fig. 1 | 53BP1 depletion promotes immune cell infiltration.** Pie chart demonstrating *TP53BP1* mRNA expression in HGSOC (a) and PDAC (b) from the TCGA. Tumor mutational burden is inversely proportional with *TP53BP1* expression in HGSOC (c) and PDAC (d) cancers.  $n = 16$  for high expression,  $n = 68$  for low expression in (c),  $n = 23$  for high expression,  $n = 24$  for low expression in (d). Box-plots represent the median and interquartile range, and the whiskers denote minimum and maximum values. Wilcoxon test. Lollipop chart demonstrating  $p$ -values for Spearman correlation between abundance of activated CD8<sup>+</sup> T-cells and expression of the indicated gene in HGSOC (e) and PDAC (f), Spearman correlation analysis. **g** Kaplan–Meier curves depicting overall survival of patients with

high or low expression of *TP53BP1*.  $n = 16$  for high expression and  $n = 68$  for low expression. **h** KEGG pathway analysis comparing RNA-sequencing profiles of KPC *Trp53bp1* KO to KPC malignant cells from subcutaneous allograft tumors from immunocompetent mice.  $n = 5$  mice per group. **i** GSEA comparing RNA-sequencing profiles of KPC *Trp53bp1* KO to KPC malignant cells from subcutaneous allograft tumors from immunocompetent mice. The vertical axis represents the top 10 ranked pathways in the Hallmark database. Interferon and inflammatory pathways are highlighted in red.  $n = 5$  mice per group. Source data are provided as a Source Data file.

engraftment model (subcutaneous). We implanted *Trp53bp1* KO KPC or *Trp53bp1* KO ID8 cells into immunocompetent mice to assess the effect of TP53BP1 loss. Consistent with TCGA data suggesting improved overall survival with low *TP53BP1* expression, loss of *Trp53bp1* inhibited tumor growth in all three mouse models (Fig. 2a–c). Intriguingly, at day 59, 12 mice out of the 15 implanted with ID8 *Trp53bp1* KO cells were without measurable tumors (Supplementary Fig. 2e). Of these 12 mice, at day 100, 9 remained without measurable tumor and apparently cured, suggesting that loss of *Trp53bp1* could elicit a sustained anti-tumor response. To further investigate this possibility, we rechallenged by subcutaneous injection of ID8 cells (Supplementary Fig. 2f). Tumor-naïve age-matched mice were used as controls. All five cured mice

exhibited complete protection from rechallenge compared to naïve animals which displayed the expected rapid tumor development demonstrating that TP53BP1 loss conferred prolonged anti-tumor response (Fig. 2d).

Induction of the adaptive immune system could explain the anti-tumor responses observed upon 53BP1 loss (Fig. 2a–c). Additionally, our interrogation of the TISIDB demonstrated decreased *TP53BP1* expression correlated with increased activated CD8<sup>+</sup> T-cell infiltration (Fig. 1e, f), and our gene expression profiling of and *Trp53bp1* KO PDAC and HGSOC tumors revealed strong enrichment of Interferon gamma (IFN- $\gamma$ ) transcriptional response signature (Fig. 1i; Supplementary Fig. 1i), where IFN- $\gamma$  is primarily produced by tumor-infiltrating



T-cells<sup>59</sup>. Thus, to confirm increased CD8<sup>+</sup> T-cell infiltration upon *Trp53bp1* loss, we performed immunohistochemistry (IHC) staining for CD8<sup>+</sup> T-cells in KPC and KPC *Trp53bp1* KO tumors and in ID8 and ID8 *Trp53bp1* KO tumors. *Trp53bp1* loss correlated with increased CD8<sup>+</sup> T-cell infiltration in both PDAC tumor engraftment models (Fig. 2e–g; Supplementary Fig. 2g). Consistently, *Trp53bp1* loss correlated with increased CD8<sup>+</sup> T-cell infiltration in the mouse HGSOC tumor

engraftment model (Supplementary Fig. 2h, i). Indeed, induction of the adaptive immune system could explain the sustained anti-tumor response seen in Fig. 2d as it has been shown that potent immunostimulatory therapies for cancer induce proliferation of memory (CD44<sup>high</sup>) CD4<sup>+</sup> and CD8<sup>+</sup> T-cells<sup>60</sup>. Therefore, we assessed T-cell phenotype by flow cytometry in the spleens of tumor-naïve age-matched mice and cured mice. Cured mice exhibited increased both CD4<sup>+</sup>



**Fig. 2 | 53BP1 depletion inhibits tumor growth and promotes immune cell infiltration.** Immunocompetent wildtype mice were injected subcutaneously (a) or orthotopically (b) with the indicated derivatives of KPC cells. Analysis of serial changes in tumor volumes.  $n = 13$  in control group and  $n = 12$  in *Trp53bp1* KO group (a),  $n = 5$  mice per group (b). c Immunocompetent wildtype mice were injected subcutaneously with the indicated derivatives of ID8 cells. Analysis of serial changes in tumor volumes.  $n = 15$  mice per group. d ID8 tumor cells were injected into age-matched immunocompetent wildtype mice or mice previously implanted with ID8 *Trp53bp1* KO tumor cells and cured. Tumor volumes at day 20 and 25.  $n = 5$  mice per group. e Representative immunohistochemistry (IHC) images for CD8<sup>+</sup> T cells. Scale bar, 0.050 mm. f Quantification of IHC data from subcutaneously implanted derivative KPC cells.  $n = 7$  mice per group. g Quantification of IHC data from orthotopically implanted derivative KPC cells.  $n = 5$  mice per group. h Nude mice were injected subcutaneously with indicated derivative KPC cells. Analysis of serial

changes in tumor volumes.  $n = 10$  mice per group. i Representative IHC images for F4/80<sup>+</sup> cells. Scale bar, 0.100 mm. j Quantification of IHC data.  $n = 7$  mice per group. k Quantification of IHC data from orthotopically implanted derivative KPC cells.  $n = 5$  mice per group. l Representative IHC images for CD86<sup>+</sup> cells. Scale bar, 0.100 mm. m Quantification of IHC data.  $n = 7$  mice per group. n Representative IHC images for Nkp46<sup>+</sup> cells. Scale bar, 0.100 mm. o Quantification of IHC data.  $n = 7$  mice per group. p NSG mice were injected subcutaneously with indicated derivative KPC cells. Analysis of serial changes in tumor volumes.  $n = 10$  mice per group. q NSG mice were injected subcutaneously with indicated derivative ID8 cells. Analysis of serial changes in tumor volumes.  $n = 10$  mice per group. Data represent mean  $\pm$  SEM; two-tailed unpaired t-test for (a, c, d, h). Data represent median, two-tailed unpaired t-test for (b, f, g, j, k, m, o). Data represent mean  $\pm$  SEM for (p, q). Source data are provided as a Source Data file.

memory T-cells (Supplementary Fig. 2j) and CD8<sup>+</sup> memory T-cells (Supplementary Fig. 2k). Collectively, these results confirmed that 53BP1 loss stimulated CD8<sup>+</sup> T-cell infiltration and inhibited tumor growth.

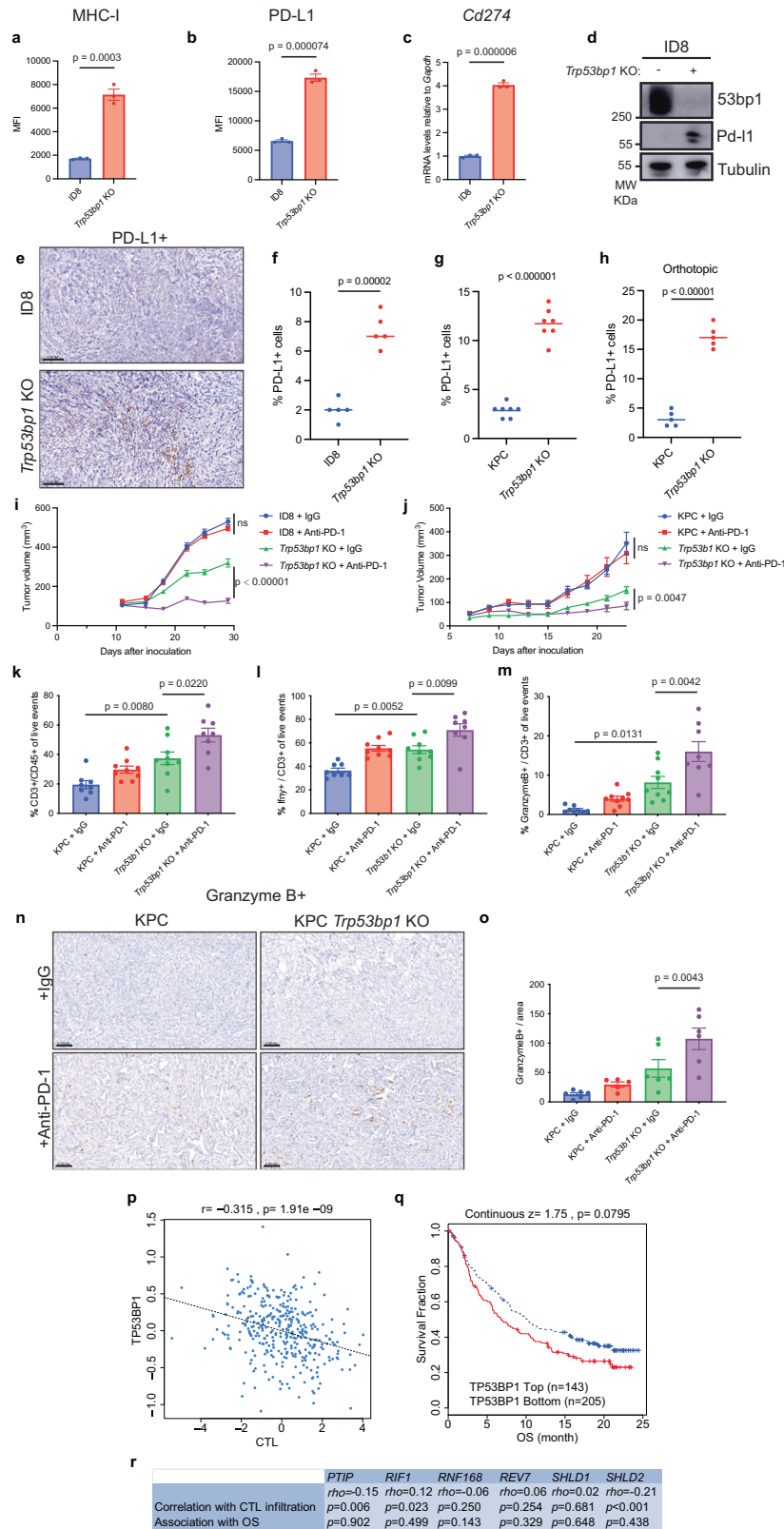
We next tested whether the interplay between TP53BP1 loss, increased interferon pathway activation, and induction of an adaptive immune response contributed to the tumor growth inhibition by implanting KPC and KPC *Trp53bp1* KO cells in immunodeficient nude (Foxn1<sup>tm</sup>) mice which lack T-cells. Remarkably, loss of *Trp53bp1* still inhibited tumor growth despite the absence of T-cells (Fig. 2h). Given IFN- $\gamma$  is also a cytokine critical to innate immunity<sup>61</sup>, we performed IHC staining to assess if components of the innate immune system were enriched in *Trp53bp1* KO tumors, explaining the continued anti-tumor response. We observed increased F4/80<sup>+</sup> macrophages in both PDAC *Trp53bp1* KO tumor engraftment models (Fig. 2i–k; Supplementary Fig. 2l) and in ID8 *Trp53bp1* KO tumors (Supplementary Fig. 2m, n). Furthermore, there was enrichment of CD86<sup>+</sup> macrophages in KPC *Trp53bp1* KO tumors and ID8 *Trp53bp1* KO tumors, consistent with an increase in anti-tumor macrophages (Fig. 2l, m; Supplementary Fig. 2o, p)<sup>62</sup>. In addition, we also observed increased NKp46<sup>+</sup> natural killer (NK) cells (Fig. 2n, o; Supplementary Fig. 2q, r). Thus, both macrophages and NK cells likely underlie the continued anti-tumor response seen in nude mice bearing KPC *Trp53bp1* KO tumors. In addition, when we interrogated the TISIDB<sup>48</sup> for the relationship between macrophages, immunomodulatory CD56<sup>bright</sup>, and cytotoxic CD56<sup>dim</sup> natural killer cells and *TP53BP1* expression in both HGSOE and PDAC, consistent with our in vivo mouse data, decreased *TP53BP1* expression correlated with increased innate immune cell infiltration (Supplementary Fig. 2s). Collectively, these data reveal that depletion of 53BP1 drives inflammatory pathway activation leading to enrichment of both innate and adaptive immune effectors. Indeed, involvement of the host immune system was necessary for the anti-tumor responses observed upon *Trp53bp1* loss (Fig. 2a–c), as implantation of KPC *Trp53bp1* KO cells or ID8 *Trp53bp1* KO cells into immunodeficient NSG mice abrogated this anti-tumor response (Fig. 2p, q).

### 53BP1 depletion upregulates immune checkpoints and cooperates with anti-PD1 antibody treatment

Anti-tumor responses induced by IFN- $\gamma$  signaling can upregulate MHC-I, critical for antigen presentation, while also upregulating immunological checkpoints, such as PD-L1<sup>63</sup>. Consequently, we first performed quantitative flow cytometry for MHC-I expression in wildtype and *Trp53bp1* KO tumors. Loss of *Trp53bp1* in ID8 ovarian tumors resulted in increased MHC-I expression (Fig. 3a). Consistently, loss of *Trp53bp1* in KPC pancreatic tumors similarly resulted in increased MHC-I expression (Supplementary Fig. 3a). Second, to explore whether the inflammatory effects mediated by 53BP1 loss could be limited by feedback activation of immunological checkpoints<sup>63</sup>, we likewise performed quantitative flow cytometry for PD-L1 expression in wildtype and *Trp53bp1* KO tumors. We observed increased PD-L1 expression

with loss of *Trp53bp1* in ID8 ovarian tumors (Fig. 3b). Similar results were also observed in KPC *Trp53bp1* KO tumors compared to wildtype tumors as well as CRISPR-mediated deletion of *TP53BP1* in the human ovarian cancer cell line COV362, and the human retinal pigment epithelial (RPE) cancer cell line (Supplementary Fig. 3b–d). In addition, CRISPR-mediated deletion of *TIRR* (*NUDT16L1*), a negative regulator of 53BP1 activity<sup>64</sup>, in a RPE cancer cell line resulted in decreased PD-L1 expression as measured by quantitative flow cytometry (Supplementary Fig. 3d). Both *Cd274* mRNA expression and PD-L1 protein expression were increased upon *Trp53bp1* loss in both ID8 (Fig. 3c, d) and KPC (Supplementary Fig. 3e, f). Finally, we observed increased PD-L1 by IHC in ID8 *Trp53bp1* KO and in both PDAC *Trp53bp1* KO tumor engraftment models (Fig. 3e–h; Supplementary Fig. 3g, h). Accordingly, we hypothesized that the anti-tumor response induced by 53BP1 loss could be improved by the addition of ICB with anti-PD-1 therapy.

Indeed, the addition of ICB with anti-PD-1 therapy significantly augmented the anti-tumor response of 53BP1 loss in both ID8 (Fig. 3i) and KPC (Fig. 3j) mouse tumor models. To explore the underlying anti-tumor response mediated by combination *Trp53bp1* loss and anti-PD-1 therapy, we performed flow cytometric analysis. Consistent with our earlier data, flow cytometric analysis demonstrated increased T-cells upon *Trp53bp1* loss and this was augmented with anti-PD-1 therapy (Fig. 3k). Similarly, flow cytometric analysis demonstrated increased IFN- $\gamma$  (Fig. 3l), and Granzyme B (Fig. 3m) expression upon *Trp53bp1* loss and this was augmented with anti-PD-1 therapy, with the latter confirmed by IHC staining for Granzyme B as well (Fig. 3n, o). To extend these findings to an independent cohort of human cancers treated with ICB, we analyzed publicly available RNA-seq data from the IMvigor210 trial, a large phase 2 trial investigating the clinical activity of PD-L1 blockade with atezolizumab in patients with metastatic urothelial cancer<sup>65</sup>. We first analyzed if infiltration of CD8<sup>+</sup> T-cells was altered based on the expression of *TP53BP1*. Consistent with our analysis of data from the TISIDB (Fig. 1e, f), in the IMvigor210 trial, decreased *TP53BP1* expression correlated with increased activated CD8<sup>+</sup> T-cell infiltration in pre-treatment biopsies (Fig. 3p). Next, we sought to explore whether low *TP53BP1* expression correlated with response to ICB and improved patient outcome. Patients from the IMvigor210 trial were stratified based on their *TP53BP1* expression as low ( $n = 205$ ) or high ( $n = 143$ ), and overall survival was assessed. We observed a non-significant but evident association of low *TP53BP1* expression and overall survival (Fig. 3q). As noted above, 53BP1 is a member of the Shieldin complex<sup>9,16,19,37,38,49–54</sup>, thus we interrogated if decreased expression of any Shieldin component would similarly correlate with response to ICB and improved patient outcome. Consistent with the importance of 53BP1, the association between response to ICB and decreased expression of other Shieldin components was weaker (Fig. 3r; Supplementary Fig. 3i, j). Taken together, these results demonstrate that TP53BP1 depletion stimulates immune checkpoints, cooperates with anti-PD1 antibody treatment, and correlates with response to ICB.



### 53BP1 depletion activates the cGAS-STING pathway

The above findings demonstrate that 53BP1 loss activates inflammatory signaling, promotes immune infiltration, leading to an anti-tumor response that can be augmented by the addition of ICB. Given 53BP1's critical role in regulating DNA end-resection, we hypothesized that this might be due to increased TMB and the production of neoantigens<sup>36,44</sup>. However, neoantigen-generated

mutational burden alone has been shown not to be sufficient to drive responsiveness to ICB<sup>66-68</sup> and the TCGA analyzed TMB for HGSOC and PDAC (Fig. 1c, d), though significantly increased with low *TP53BP1* expression, remained below a TMB of 10 mutations per megabase, the current FDA threshold for tumor agnostic use of ICB<sup>69</sup>. Rather, the increased DNA end-resection that occurs upon 53BP1 loss (Supplementary Fig. 1a, b) could lead to increased

**Fig. 3 | 53BP1 depletion upregulates immune checkpoints and synergizes with anti-PD1 antibody treatment.** Quantitative flow cytometry mean fluorescence intensity (MFI) for MHC-I (a) and PD-L1 (b) positivity from ID8 or ID8 *Trp53bp1* KO tumors. *n* = 3 mice per group. c mRNA expression of *Cd274* from ID8 or ID8 *Trp53bp1* KO tumors. mRNA expression was normalized to *Gapdh*. *n* = 3 mice per group. d Western blot analysis of PD-L1 in ID8 and ID8 *Trp53bp1* KO cells. 3 biological replicates. e Representative IHC images for PD-L1<sup>+</sup> cells from indicated derivative ID8 tumors. Scale bar, 0.100 mm. f Quantification of IHC data from 3e. *n* = 5 mice per group. Quantification of IHC data from subcutaneously (g) or orthotopically (h) implanted derivative KPC cells. *n* = 7 mice per group (g), *n* = 5 mice per group (h). Immunocompetent wildtype mice were injected subcutaneously with the indicated derivatives of ID8 (i) or KPC (j) cells and treated with vehicle or anti-PD-1 antibody. *n* = 10 in IgG group and *n* = 11 in other three groups (i), *n* = 11 in IgG

group and *n* = 12 in other three groups (j). Tumors from 3j were analyzed by flow cytometry for CD3<sup>+</sup> (k), Ifn- $\gamma$  (l), and Granzyme B (m). *n* = 8–9 mice per group. n Representative IHC images for Granzyme B<sup>+</sup> cells. Scale bar, 0.100 mm. o Quantification of IHC data. *n* = 6 mice per group. p Dotplot with Spearman correlation test of abundance of activated CD8<sup>+</sup> T-cells in pre-treatment biopsies of patients enrolled in the IMvigor210 trial in correlation to *TP53BP1* mRNA expression level. q Kaplan–Meier curves depicting overall survival of patients with high (*n* = 143) or low (*n* = 205) expression of *TP53BP1* treated with anti-PD1 therapy in patients from the IMvigor210 trial. r Association between expression of other genes in the Shieldin complex with CTL and overall survival. Data represent mean  $\pm$  SEM; two-tailed unpaired t-test for (a–c, i, j). Data represent median, two-tailed unpaired t-test for (f–h). Data represent mean  $\pm$  SEM; one-way ANOVA for (k–m, o). Source data are provided as a Source Data file.

cytosolic DNA sensing and activation of the cytosolic DNA sensor cyclic GMP-AMP synthase (cGAS)<sup>70</sup>.

To explore this possibility, we first performed immunofluorescence (IF) imaging for micronuclei, which are a known source of cytosolic DNA that can activate the cGAS-STING pathway<sup>31,32,71,72</sup> as well as total cytosolic dsDNA. Loss of 53BP1 led to a significant increase in both micronuclei (Fig. 4a; Supplementary Fig. 4a–c) and cytosolic dsDNA (Fig. 4b) and are bound by cGAS (Fig. 4c). As cGAS activation generates the second messenger, cyclic dinucleotide cyclic GMP-AMP (cGAMP) leading to induction of the STING pathway<sup>73</sup>, we next assessed cGAMP production by ELISA upon loss of 53BP1. Loss of 53BP1 led to a significant increase in cGAMP production in both ID8 and KPC cell lines (Fig. 4d, e). Third, to establish dependence on cGAS-STING pathway activation for the anti-tumor effect of TP53BP1 loss, we generated *Sting* KO and *Trp53bp1 Sting* double knockout (DKO) cells in both the ID8 ovarian and KPC pancreatic cancer models (Fig. 4f). Loss of *Trp53bp1* resulted in phosphorylation of Tbk1 and *Sting*, and increased expression of Pd-I1 (Fig. 4f). Whereas loss of *Sting* abrogated phosphorylation of Tbk1 and the increased Pd-I1 expression seen upon *Trp53bp1* loss in both ID8 and KPC (Fig. 4f). We then determined if *Sting* loss would prevent the activation of inflammatory pathways by assessing the mRNA expression of a panel of inflammatory genes (*Cd274*, *Ccl5*, and *Ifnb1*) whose expression increased upon *Trp53bp1* loss. As predicted, quantitative polymerase chain reaction (qPCR) analysis demonstrated that the increased mRNA expression of these genes was abrogated upon *Sting* loss (Fig. 4g). Because cGAS independent activation of STING has been previously shown<sup>74</sup>, to establish dependence on cGAS-STING pathway activation for the anti-tumor effect of TP53BP1 loss, we generated *Trp53bp1 Cgas* DKO cells in both the ID8 ovarian and KPC pancreatic cancer models (Supplementary Fig. 4e, f). Confirming the anti-tumor effect of TP53BP1 loss is mediated by cGAS-STING pathway activation, loss of *Cgas* abrogated phosphorylation of *Sting* and Tbk1 (Supplementary Fig. 4e, f). Consistently, loss of *Cgas* abrogated the increased mRNA expression of a panel of inflammatory genes seen upon *Trp53bp1* loss (Supplementary Fig. 4g, h). These results demonstrate that *Trp53bp1* loss activates cGAS-STING signaling.

Given the critical role of 53BP1 in DSB repair, where it prevents DNA end-resection to promote NHEJ, we hypothesized that DNA end-resection would be necessary for activation of the cGAS-STING pathway. Consistent with loss of TP53BP1 leading to increased DNA end-resection (Supplementary Fig. 1a, b), depletion of the *Mre11* or *Exo1*, two nucleases involved in DNA end-resection<sup>75</sup> reduced activation of the cGAS-STING pathway upon *Trp53bp1* loss (Fig. 4h–k; Supplementary Fig. 4i, j). Finally, we hypothesized that loss of *Sting* would abrogate the anti-tumor responses observed upon *Trp53bp1* loss (Fig. 2a–c). To that end, we subcutaneously injected ID8 *Trp53bp1* KO or ID8 *Trp53bp1 Sting* DKO cells into immune competent syngeneic animals resulting in allograft tumors and performed IHC. Loss of a *Sting* in 53bp1-deficient significantly decreased Pd-I1 by IHC (Fig. 4l, m) and decreased CD8<sup>+</sup> T-cell (Fig. 4n, o), F4/80<sup>+</sup> macrophages (Supplementary Fig. 4k, l), CD86<sup>+</sup> macrophages

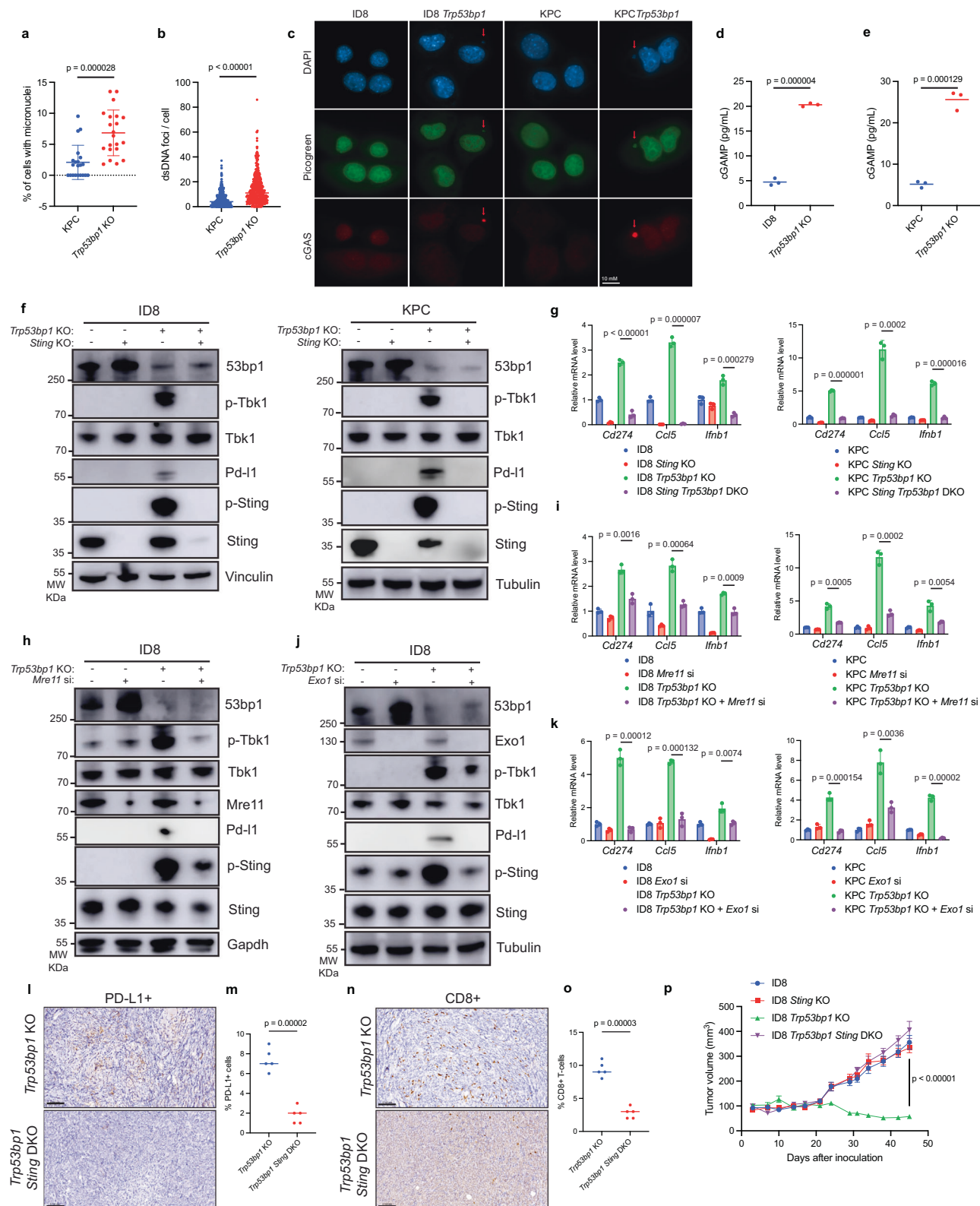
(Supplementary Fig. 4m, n), and Nkp46<sup>+</sup> NK cells (Supplementary Fig. 4o, p) infiltration. Collectively, these results strongly suggest that loss of 53BP1 leads to the production of cytosolic DNA due to increased DNA end-resection, and this activates the cGAS-STING pathway leading to a pro-inflammatory response, which is abrogated by decreased DNA end-resection. Indeed, activation of cGAS-STING pathway was necessary for the anti-tumor responses observed upon *Trp53bp1* loss (Fig. 2a–c), as loss of *Sting* abrogated the anti-tumor response observed upon *Trp53bp1* loss (Fig. 4p).

### 53BP1 loss mediated PARP inhibitor resistance is overcome with anti-PD1 antibody treatment

We have established that 53BP1 loss leads to increased DNA end-resection which activates the cGAS-STING pathway leading to increased inflammatory signaling, immune cell infiltration, and inhibition of tumor growth which can be enhanced by the addition of ICB. To expand the clinical relevance of our findings and given loss of 53BP1 is a mechanism of resistance to PARP inhibitors (PARPi) in BRCA1-deficient cancers<sup>9,16,19,34–39</sup>, we hypothesized that loss of TP53BP1 in BRCA1-deficient cancers while inducing resistance to PARPi, would increase sensitivity to ICB. To that end, we generated KPC *Brcal* KO and KPC *Brcal Trp53bp1* DKO cells, and ID8 *Brcal* KO and ID8 *Brcal Trp53bp1* DKO cells (Fig. 5a; Supplementary Fig. 5a). As predicted, loss of *Trp53bp1* rendered the *Brcal* KO cells resistant to PARPi treatment with Olaparib (Fig. 5b; Supplementary Fig. 5b). The *Brcal Trp53bp1* DKO cells had significantly more micronuclei (Supplementary Fig. 5c, d), DNA end-resection (Supplementary Fig. 5e), increased expression of *Cd274*, *Ccl5*, and *Ifnb1* (Fig. 5c; Supplementary Fig. 5f), and activation of cGAS-STING pathway signaling (Supplementary Fig. 5g). We next subcutaneously injected KPC *Brcal* KO or KPC *Brcal Trp53bp1* DKO cells into immune competent syngeneic animals resulting in allograft tumors and performed IHC. Loss of *Trp53bp1* in a *Brcal*-deficient setting significantly increased the proportion of CD8<sup>+</sup> T-cells (Fig. 5d), F4/80<sup>+</sup> macrophages (Fig. 5e), CD86<sup>+</sup> anti-tumor macrophages (Fig. 5f), Nkp46<sup>+</sup> natural killer cells (Fig. 5g) and Pd-I1 expression (Fig. 5h), consistent with the increased immune cell infiltration seen in PARPi-resistant BRCA1-KO tumors<sup>76</sup>. Additionally, RNA extracted from KPC *Brcal Trp53bp1* DKO tumors demonstrated increased mRNA expression of *Cd274*, *Ccl5*, and *Ifnb1* (Fig. 5i). These results demonstrate that *Trp53bp1* loss in a murine model of *Brcal*-deficient pancreatic cancer led to increased DNA end-resection, activation of inflammatory signaling and innate and adaptive immune cell infiltration.

Accordingly, we hypothesized that loss of *Trp53bp1* in a murine model *Brcal*-deficient pancreatic cancer would increase sensitivity to ICB and rescue PARPi resistance. We subcutaneously injected KPC *Brcal* KO or KPC *Brcal Trp53bp1* DKO cells into immune competent syngeneic animals and tumor-bearing mice were treated with PARPi (Olaparib) and anti-PD-1 therapy. Consistent with our data demonstrating that loss of 53BP1 sensitizes cancers to ICB (Fig. 3), anti-PD-1 therapy inhibited KPC *Brcal Trp53bp1* tumor growth (Fig. 5j;





Supplementary Fig. 5h). In addition, anti-PD-1 therapy re-sensitized the PARPi-resistant KPC *Brca1 Trp53bp1* to Olaparib (Fig. 5j). Whereas Olaparib-treated and vehicle-treated mice bearing KPC *Brca1 Trp53bp1* tumors showed comparable growth in tumor volume, combination Olaparib and anti-PD-1 therapy significantly inhibited tumor growth (Fig. 5j). Together, these data suggest that 53BP1 deficient tumors are vulnerable to ICB and this can be exploited to overcome PARPi resistance in BRCA1-mutant tumors.

## Discussion

In DSB repair, 53BP1 is the counterpart to BRCA1, where it regulates the choice between NHEJ and HR, promoting end-joining by NHEJ, and preventing DNA end-resection which would lead to repair by HR<sup>54</sup>. Surprisingly, despite this key DSB repair role, analysis of TCGA datasets for HGSOc demonstrated that decreased *TP53BP1* expression correlated with improved overall survival. Given 53BP1 prevents DNA end-resection, we hypothesized that tumors with decreased *TP53BP1*



**Fig. 4 | 53BP1 depletion activates the cGAS-STING pathway.** **a** Quantification of IF data for the indicated cell lines. Representative IF images in Supplementary Fig. 4a.  $n = 21$  cells counted per group. **b** Quantification of cytoplasmic dsDNA foci in indicated cell lines ( $n = 488$  cells). **c** Representative IF images for the indicated cell lines demonstrating cGAS-bound micronuclei. 3 biological replicates. **d** 2'3'-cGAMP levels by ELISA in the indicated ID8 derivative (**d**) and KPC derivative (**e**) cell lines  $n = 3$  independent experiments. **f** Western blot analysis of PD-L1 expression and cGAS-STING pathway activation in the indicated ID8 derivatives (left panel) or the indicated KPC derivatives (right panel). **g** mRNA expression of *Cd274*, *Ccl5*, and *Ifnb1*, in the indicated ID8 derivatives (left panel) or the indicated KPC derivatives (right panel). mRNA expression was normalized to *Actb*.  $n = 3$  independent experiments. **h** Western blot analysis of PD-L1 expression and cGAS-STING pathway activation in the indicated ID8 derivatives. **i** mRNA expression of *Cd274*, *Ccl5*, and *Ifnb1*, in the indicated ID8 derivatives (left panel) or the indicated KPC derivatives (right panel). mRNA expression was normalized to *Actb*.  $n = 3$  independent

experiments. **j** Western blot analysis of PD-L1 expression and cGAS-STING pathway activation in the indicated ID8 derivatives. 3 independent experiments for (**f**, **h**, **j**). **k** mRNA expression of *Cd274*, *Ccl5*, and *Ifnb1*, in the indicated ID8 derivatives (left panel) or the indicated KPC derivatives (right panel). mRNA expression was normalized to *Actb*.  $n = 3$  independent experiments. **l** Representative IHC images for PD-L1<sup>+</sup> cells from indicated derivative ID8 *Trp53bp1* KO tumors. Scale bar, 0.100 mm. **m** Quantification of IHC data.  $n = 5$  mice per group. **n** Representative IHC images for CD8<sup>+</sup> T-cells from indicated derivative ID8 *Trp53bp1* KO tumors. Scale bar, 0.100 mm. **o** Quantification of IHC data.  $n = 5$  mice per group. **p** Immunocompetent wildtype mice were injected subcutaneously with indicated derivative ID8 cells. Analysis of serial changes in tumor volumes.  $n = 10$  mice per group. Data represent mean  $\pm$  SD; two-tailed unpaired t-test for (**a**, **b**, **g**, **i**, **k**). Data represent median, two-tailed unpaired t-test for (**d**, **e**, **m**, **o**). Data represent mean  $\pm$  SEM; two-tailed unpaired t-test for (**p**). Source data are provided as a Source Data file.

expression would have increased TMB and therefore increased immune cell infiltration and activated antitumor immunity. Analysis of TCGA datasets for HGSOc and PDAC demonstrated increased TMB with decreased *TP53BP1* expression. Interrogation of the TISIDB confirmed increased infiltration of activated CD8<sup>+</sup> T-cells and activation of macrophages and NK cells in HGSOc and PDAC tumors with decreased *TP53BP1* expression. Given the TISIDB integrates multiple heterogeneous data types, we verified the relationship between 53BP1 expression and CD8, PD-L1, and Nkp46 by performing multicolor IF on a tissue microarray of HGSOc and PDAC tissue samples (Fig. 6; Supplementary Fig. 6). The HGSOc tissue microarray consisted of 4 patients with stage IA, 2 patients with stage IB, 9 patients with stage II, 2 patients with stage IIIA2, and 28 patients with stage IIIC disease. The PDAC tissue microarray consisted of 4 patients with stage IA, 10 patients with stage IB, 15 patients with stage IIA, 11 patients with stage IIB, and 5 patients with stage III disease. Multicolor IF allowed interrogation of 53BP1 protein expression and low 53BP1 expression correlated with increased CD8<sup>+</sup> T-cell (Fig. 6b, e) and Nkp46<sup>+</sup> NK cell (Fig. 6c, f) infiltration. In addition, low 53BP1 expression correlated with increased PD-L1 expression (Fig. 6d, g). This suggested that immune-regulated mechanisms might contribute to the antitumor response seen in tumors with decreased *TP53BP1* expression and might facilitate response to ICB. Indeed, analysis of the IMvigor210 trial, demonstrated that lower *TP53BP1* expression correlated with enhanced response to ICB and improved patient outcome. Importantly, despite 53BP1 being a member of the Shieldin complex, expression of other DSB end-protection factors did not associate with increased immune infiltration or improvement in overall survival, and did not predict response to ICB, reinforcing the importance of 53BP1 as the primary counterpart of BRCA1 and its critical role in DSB repair. Unfortunately, there have been no immunotherapy trials involving patients with PARPi resistant BRCA-mutated ovarian tumors to directly test our hypothesis. However, our results indicate that patients with PARPi-resistant BRCA1-mutated 53BP1 loss cancers might benefit from a combination of PARPi and immunotherapy. This indicates the feasibility of initiating clinical trials to explore the use of immunotherapy in patients with PARPi resistant BRCA-mutated and 53BP1 loss ovarian tumors. This line of investigation not only holds promise for offering hope to patients with these types of tumors but also contributes to expanding therapeutic strategies for ovarian cancer.

To confirm our findings and to elucidate how decreased *TP53BP1* expression enhanced immunogenicity and improved overall survival, we developed mouse models of *Trp53bp1* KO HGSOc and PDAC that recapitulated our findings of decreased tumor growth, immune cell infiltration, and increased sensitivity to ICB. Transcriptomic analysis demonstrated upregulation of cytokine signaling and inflammatory pathways. We hypothesized that given 53BP1's role in negatively regulating DNA end-resection, loss of 53BP1 resulting in increased end-resection would yield chromosome abnormalities, micronuclei

production, and leak of nuclear DNA into the cytoplasm leading to cGAS-STING pathway activation and upregulation of cytokine signaling and inflammatory pathways. Indeed, *Trp53bp1* depletion led to a significant increase in micronuclei and cytoplasmic dsRNA resulting in activation of cGAS-STING signaling. Consistently, depletion of two nucleases involved in DNA end-resection, Mre11 or Exo1<sup>75</sup>, abrogated cGAS-STING pathway activation upon *Trp53bp1* loss. Moreover, we observed upregulation of Pd-l1 upon *Trp53bp1* loss which was abrogated upon *Sting* depletion. Altogether, these data support a model where 53BP1 deficiency leads to increased DNA end-resection, activation of cGAS-STING signaling, and PD-L1 expression to facilitate response to ICB.

Finally, loss of 53BP1 is a mechanism of resistance to PARPi in BRCA1-deficient cancers<sup>9,16,19,34–39</sup>. Indeed, loss of 53BP1 was recently reported to be the most frequent alteration that drives spontaneous resistance to PARPi in an in vivo model system<sup>76</sup>. In this setting, upregulation of genes associated with IFN $\gamma$  and increased immune infiltration was observed, suggesting induction of cGAS-STING signaling, consistent with our data (Fig. 5). Indeed, we show that loss of 53BP1 re-sensitized BRCA1-deficient pancreatic cancer to PARPi when combined with ICB. These findings may also explain results of recent clinical trials of combined PARP and PD-(L)1 blockade in BRCA1-mutated tumors showing that PARPi/PD-(L)1i may increase duration of response to PARPi therapy<sup>77</sup>, likely by overcoming acquired resistance due to 53BP1 loss.

In conclusion, we demonstrate a link between decreased 53BP1 expression, immunogenicity, improved survival, and response to ICB in HGSOc and PDAC, supporting inclusion of 53BP1 expression as an exploratory biomarker in trials of ICB in these cancers. Loss of 53BP1 has been shown to be a frequent alteration and cause of PARPi resistance in BRCA1-mutated tumors<sup>76</sup>, and we demonstrate that resistance to PARPi can be overcome with ICB, suggesting that patients with PARPi-resistant BRCA1-mutated cancers might benefit from PARPi and immunotherapy combination. Furthermore, our results support development of 53BP1 inhibitors (protac-based or otherwise) as a strategy to prime immunologically “cold” tumors (such as ovarian and pancreatic cancers) for response to immunotherapy.

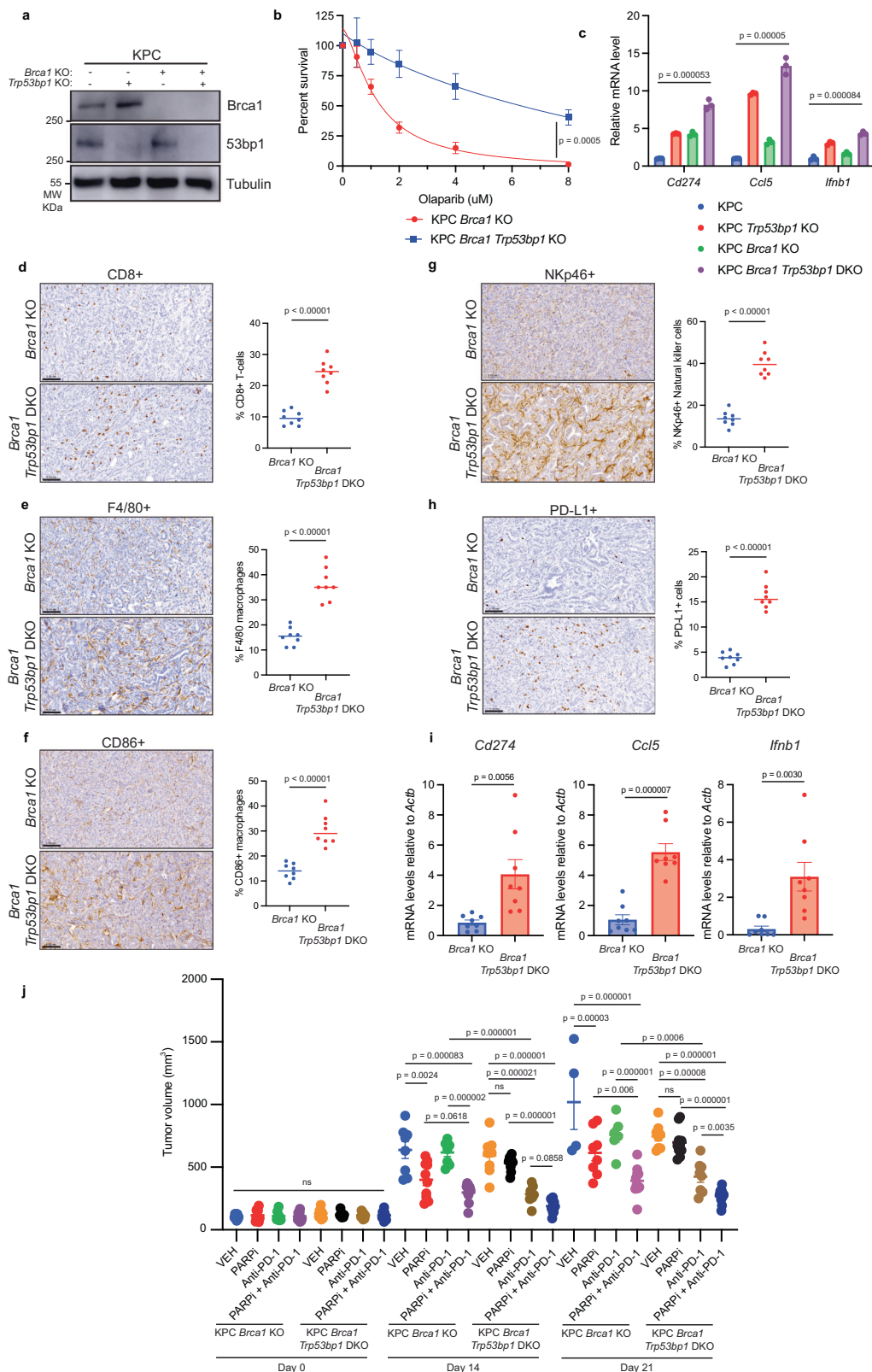
## Methods

### Ethical statement

This research complies with all relevant ethical regulations. All animal experiments were approved by the Institutional Animal Care and Use Committee at the Dana-Farber Cancer Institute (Protocol 08-036).

### Cell lines

The murine ovarian cancer cell line, ID8, was a gift from Weiping Zou and was derived as previously described<sup>26</sup>. ID8 cells were cultured in RPMI 1640 (Gibco) media, supplemented with 10% fetal bovine serum (FBS), 100 U/mL penicillin, and streptomycin. The murine pancreatic



cancer cell line, KPC (*Kras*<sup>LSL-G12D</sup>; *Trp53*<sup>LoxP</sup>; *Pdx1-Cre*; *Rosa26YFP/YFP*) was derived from late-stage primary tumors from an autochthonous mouse model of *Kras* and *Trp53*-mutated PDAC, as previously described<sup>57</sup>. KPC cells were cultured in DMEM (Gibco), supplemented with 10% FBS. Cov362 cell, and RPE1 cell lines were obtained from American Tissue Culture Collection (ATCC), and cultured in DMEM (Gibco), supplemented with 10% FBS. All cell lines were regularly tested for *Mycoplasma* using MycoAlert Mycoplasma Detection Kit from

Lonza. All cell lines were identified by the DFCI Molecular Diagnostics Core Human Cell Line Authentication service at periodic intervals during the course of the study.

### CRISPR/Cas9 knockout generation

Knockout (KO) cancer cell lines were generated by transfecting cells with TrueCut Cas9 protein and TrueGuide synthetic RNA using Lipofectamine CRISPRMax (Life Technologies) according to the

**Fig. 5 | 53BP1 loss mediated PARP inhibitor resistance is overcome with anti-PD-1 antibody treatment.** **a** Western blot analysis demonstrating generation of KPC *Bracl1* KO and KPC *Bracl1 Trp53bp1* double knockout (DKO) cells. **b** Quantification of clonogenic survival assay with KPC *Bracl1* KO and KPC *Bracl1 Trp53bp1* DKO cells, treated with PARP inhibitor (Olaparib). Data are represented as mean  $\pm$  SD; two-tailed unpaired t-test of highest dose. 3 independent experiments for (a, b). **c** mRNA expression of *Cd274*, *Ccl5*, and *Ifrnb1*, in the indicated cell lines. mRNA expression was normalized to *Actb*.  $n = 3$  independent experiments. Data represent mean  $\pm$  SD; two-tailed unpaired t-test. **d** Left: representative IHC images for CD8<sup>+</sup> T cells. Scale bar, 0.100 mm. Right: quantification of IHC data.  $n = 8$  mice per group. **e** Left: representative IHC images for F4/80<sup>+</sup> cells. Scale bar, 0.100 mm. Right: quantification of IHC data.  $n = 8$  mice per group. **f** Left: representative IHC images for CD86<sup>+</sup> cells. Scale bar, 0.100 mm. Right: quantification of IHC data.  $N = 8$

mice per group. **g** Left: representative IHC images for Nkp46<sup>+</sup> cells. Scale bar, 0.100 mm. Right: quantification of IHC data.  $n = 8$  mice per group. **h** Left: representative IHC images for PD-L1<sup>+</sup> cells. Scale bar, 0.100 mm. Right: quantification of IHC data.  $n = 8$  mice per group. **i** mRNA expression of *Cd274*, *Ccl5*, and *Ifrnb1* from KPC *Bracl1* KO and KPC *Bracl1 Trp53bp1* DKO tumors. mRNA expression was normalized to *Actb*.  $n = 8$  mice per group. Data represent median; two-tailed unpaired t-test for (d–i). **j** Immunocompetent wildtype mice were injected subcutaneously with KPC *Bracl1* KO or KPC *Bracl1 Trp53bp1* DKO cells and treated with vehicle (IgG) PARP inhibition (PARPi, Olaparib), anti-PD-1 antibody, or the combination of PARPi and anti-PD-1. Analysis of tumor volumes at Day 0, Day 14, and Day 21 of treatment.  $n = 8$  in VEH and anti-PD-1 groups and  $n = 10$  in the other groups were initially inoculated. Data represent mean  $\pm$  SEM; one-way ANOVA analysis with Sidak post hoc test. Source data are provided as a Source Data file.

manufacturer's protocol or by the CRISPR-based multi-guide Gene Knockout Kit v2 (Synthego) according to the manufacturer's protocol. 48 h after transfection, single cell sorting was performed by the Dana-Farber Cancer Institute Flow Cytometry Core, and Western blot analysis was used to select successful KOs. TrueGuide synthetic gRNAs were purchased from Thermo. For *Trp53bp1* editing, two guides were employed: *UGCCAAUGGAGUCGGUUUG*, and *UUAGGUUACUGAAGGUCAU*. For *Trp53* editing, two guides were employed: *CUGUGAGCCUCCGAAGUGA*, and *UAUUCGGACUUUUACAGAGG*. For *Bracl1* editing, three guides were employed: *UUCAUGCAAUGAGUAGCAG*, *CUUCUGUUGACUUACCAGAU*, and *CAUUUUGUACUUUCUUGAAUU*. For *Tmem173* editing, three guides were employed: *GCGAGGCUAGGUGAAGUGCU*, *GAUGAUCCUUUGGGUGGCAA*, and *ACCUGCAUCCAGCAUCCCA*. For *Cgas* editing, three guides were employed: *GGCCCCGAGUGCAUCCAGCA*, *CGCGGGGGCGGAGCGUGAC*, and *CAGCAGGACCAGGGCCCCAGC*.

### Animal experiments

All animal experiments were approved by the Institutional Animal Care and Use Committee at the Dana-Farber Cancer Institute (Protocol 08-036). Animals were housed in the Dana-Farber Cancer Institute Animal Resource Facility under controlled environmental conditions (temperature: 20  $\pm$  2 °C; humidity: 35  $\pm$  10%; photoperiod: 12 h light/12 h dark; HEPA-filtered air; animals enclosures provided sterile and adequate space with bedding material, food and water, environmental and social enrichment). All mice (C57BL/6J wild-type, NOD.Cg-*Prkdc*<sup>scid</sup>*Il2rg*<sup>tm1Wjl/SzJ</sup>, B6.Cg-*Foxn1*<sup>nu/J</sup>) were purchased from Jackson Laboratories. Female mice aged at least 6 weeks were used for all experiments. For the subcutaneous tumor model,  $1.5 \times 10^6$  tumor cells (0.050 mL) were resuspended in PBS and mixed 1:1 with Matrigel (Corning) and injected subcutaneously into the right flanks of mice. For the orthotopic tumor model, an incision was made in the skin and peritoneum of anesthetized mice, and the pancreas was externalized.  $1 \times 10^5$  tumor cells (0.030 mL) were resuspended in PBS and mixed 1:1 with Matrigel (Corning) and injected into the tail of the pancreas. The pancreas was then reinserted, and the skin was sutured. For immunotherapy studies, tumor-bearing mice were randomly apportioned into different treatment groups (IgG2a or anti-PD-1 antibody) once the tumors were palpable and reached a volume of 50 to 100 mm<sup>3</sup>. Anti-PD-1 (Bio X Cell; BP0273) and IgG2a isotype (Bio X Cell; BP0089) were administered intraperitoneally at 10 mg/kg every other day for a total of 3 doses. For combination PARPi and immunotherapy studies, tumor-bearing mice were randomly apportioned into different treatment groups (IgG2a, Anti-PD-1 antibody, Olaparib, combination Olaparib + IgG2a, or combination Olaparib + Anti-PD-1 antibody). Olaparib (Selleckchem; S1060) was administered intraperitoneally at 50 mg/kg daily. Anti-PD-1 (Bio X Cell; BP0273) and IgG2a isotype (Bio X Cell; BP0089) were administered intraperitoneally at 10 mg/kg twice a week. Subcutaneous tumor growth was measured every 3 to 4 days using electronic calipers, and tumor volumes were calculated as follows:  $V = (W^2 \times L)/2$ . For the subcutaneous model, tumor

measurements continued until tumors reached either 2000 mm<sup>3</sup> in volume or became ulcerated, at which point, the mice were humanely euthanized. For the orthotopic model, mice were sacrificed at 21 days post-surgery and tumors were weighed.

### Western blot

Cells were harvested and lysed in buffer containing 150 mM NaCl, 20 mM HCl [pH 7.5], 0.5% NP-40, 5 mM EDTA, 5% glycerol, and supplemented with protease and phosphatase cocktail inhibitors (Roche) for 30 minutes on ice in a 4 °C cold room. Protein concentration was measured using the Bradford assay (23225, ThermoFisher Scientific). 20  $\mu$ g lysate was mixed with SDS loading buffer and loaded into 4%–12% precast gels (NP0335, Life Technologies). After transferring the protein to the membranes by Tris-Glycine wet transfer, membranes were blocked with 5% milk in TBST for 1 h at room temperature. Membranes were incubated with appropriate primary antibodies (Supplementary Table 1) at room temperature for 1 h or overnight in a 4 °C cold room. Appropriate enhanced chemiluminescence secondary antibodies (Supplementary Table 1), were then applied for 1 h at room temperature. Membranes were developed using Western Lightning (Perkin Elmer) and imaged on an AI600 Chemiluminescent Imager (Amersham).

### DNA end-resection assay

To quantify DNA end-resection, U2OS cells stably expressing ER-AsiSI were employed. Cells were transfected with control siRNA or siRNA targeting *TP53BP1* 48 h prior to treatment either with or without 300 nM 4-OHT to induce DSBs at specific AsiSI cut sites by allowing transportation of the constitutively expressed AsiSI to the nucleus. After four hours, genomic DNA was extracted with the DNeasy Blood & Tissue Kit (Qiagen). Genomic DNA was either mock digested or digested overnight with BsrGI-HF (New England Biolabs). Digested or mock-digested samples (2  $\mu$ l) were used as templates in a qPCR reaction containing 10  $\mu$ l of 2 $\times$  SYBR green (ThermoFisher), and 1  $\mu$ M of each primer using a QuantStudio 7 Real-Time PCR System (ThermoFisher). The single-stranded DNA percentage (ssDNA%) generated by resection was determined by calculating a  $\Delta$ Ct for each sample: the Ct value of the mock-digested sample was subtracted from the Ct value of the digested sample.

### Immunohistochemistry (IHC)

IHC was performed on tumors fixed overnight using 10% formalin solution. Tumors were embedded, sectioned, and stained by iHisto. Stained slides were scanned at 40X magnification.

### Immunofluorescence (IF)

Cells were seeded on the coverslips and fixed the following day in 4% formaldehyde for 10 min at room temperature. Fixed cells were permeabilized with 0.1% Triton X-100 for 5 min. Coverslips were washed twice and then incubated with the appropriate primary antibody (Supplementary Table 1) for 1 h at room temperature. Following



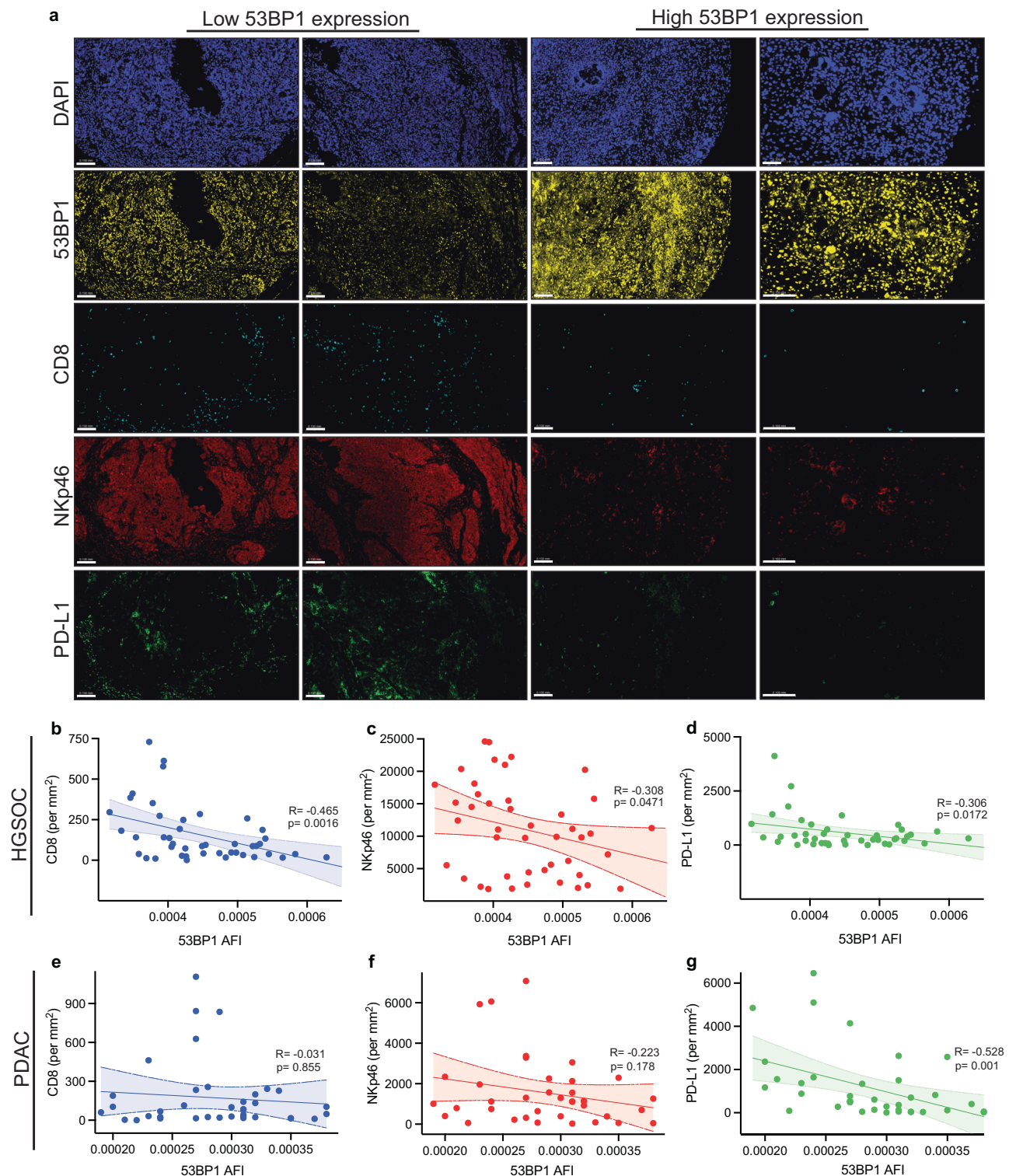


**Fig. 6 | Low 53BP1 expression correlates with increased immune cell infiltration in HGSOc and PDAC.** **a** Representative IF images processed for DAPI, 53BP1, CD8, NKp46, and PD-L1 from an independent cohort of 45 HGSOc tissue samples. 45 samples analyzed. Dotplot with Spearman correlation test of abundance of CD8<sup>+</sup> T-cells (**b**), NKp46 NK cells (**c**) and PD-L1 expression (**d**) CD8<sup>+</sup> T-cells in 45 HGSOc

tissue samples in correlation to TP53BP1 protein expression level. Dotplot with Spearman correlation test of abundance of CD8<sup>+</sup> T-cells (**e**), NKp46 NK cells (**f**) and PD-L1 expression (**g**) in 38 PDAC tissue samples in correlation to TP53BP1 protein expression level. Spearman correlation analysis was performed for (**b–g**). Source data are provided as a Source Data file.

incubation with the primary antibody, coverslips were washed three times and incubated with the appropriate fluorescent secondary antibody for 1 h at room temperature. Coverslips were washed three times and then mounted on glass slides using Prolong Gold mounting reagent with DAPI (p36931, Invitrogen). Cells were imaged by an

Olympus BX41 microscope equipped with a digital camera at 63x magnification and quantified using Image J (NIH). To determine the amount of cytoplasmic dsDNA, cells (either KPC or COV362 cells) were seeded onto 18 mm round optical coverslips. Following a PBS wash, the cells were fixed with 4% paraformaldehyde for 20 min at room



temperature. Subsequently, selective permeabilization of the plasma membrane was achieved by incubating the cells with 0.05% saponin in PBS for 5 min. After three additional PBS washes, the cells were blocked using 3% BSA in PBS for 1 h. To detect dsDNA, the cells were subjected to a 2-h incubation with an anti-dsDNA antibody (Abcam, ab27156). This was followed by three washes using 0.05% Triton X-100 in PBS. Next, the cells were incubated with an anti-mouse antibody conjugated with Alexa Fluor™ 488 (Invitrogen, A-11001) for 1 h. Images were analyzed by using CellProfiler software (Version 4.2.5) for quantification of dsDNA foci.

### Tissue microarray multicolor immunofluorescence

The tissue microarray utilized for multicolor IF included 46 samples of HGSOc and three normal ovarian samples, with 45 HGSOc samples analyzed (Bioaitech, cat.no. F049Ov01, Xi'an, China). For PDAC, the tissue microarray included 45 samples of PDAC and four normal samples, with 38 PDAC samples analyzed (Bioaitech, cat.no. D049Pa01, Xi'an, China). The tissue microarrays were purchased from Bioaitech. The study using the tissue microarray was approved by the Life Sciences Ethics Committee of Changsha Yaxiang Biotechnology Co., LTD. The Ethics report is available online at [yxswll.ccrl.cn](http://yxswll.ccrl.cn). The query code is 8KF4GPGVSI1MLV8. The tissue slices underwent routine dewaxing, followed by antigen retrieval using Tris-EDTA Buffer solution, inactivation of endogenous peroxidase with 3% H<sub>2</sub>O<sub>2</sub>, and blocking with goat serum. Subsequently, the slides were incubated overnight with primary antibodies NKp46 (ZEN-Bioscience, R51204), PD-L1 (Abcam, ab213524), 53BP1 (ZEN-Bioscience, R381816), and CD8 (Abcam, ab245118). Following this, they were incubated with an HRP-labeled goat anti-rabbit/mouse secondary antibody. Target proteins were labeled with specific fluorescence using tyramide signal amplification (TSA). For this purpose, TSA-CY3, TSA-488, TSA-430, and TSA-594 were respectively employed for NKp46, PD-L1, 53BP1, and CD8. Finally, the slides were incubated with DAPI for 1 h at room temperature.

### Flow cytometry

To analyze changes in the tumor microenvironment, subcutaneous tumors were harvested and digested with collagenase and hyaluronidase for 1 h in a 37 °C cell incubator. Tumors were then finely minced and passed through cell strainers to achieve a single cell suspension. Red blood cells were depleted using RBC lysis buffer (ThermoFisher Scientific), and samples resuspended in fluorescence-activated cell sorting (FACS) buffer. Cells were incubated with anti-mouse CD16/CD32 Fcγ receptor II/III blocking antibody and Zombie Violet Viability kit (Biolegend) for 15 min at room temperature before incubating with surface antibodies. Surface antigens were stained with the indicated antibodies (Supplementary Table 2) at 4 °C for 30 min. Cells were fixed and permeabilized before incubating with antibodies for intracellular antigens as indicated in Supplementary Table 2. Cells were then washed, resuspended in PBS, and analyzed using a BD LSR Fortessa flow cytometer in the Dana-Farber Cancer Institute Flow Cytometry Core. See Supplementary Fig. 7 for gating strategy. Analysis was performed using FlowJo 10 and GraphPad Prism 9.0.

### Real-time quantitative polymerase chain reaction (RT-qPCR)

Total RNA was isolated using Qiagen RNeasy kit (#74004). RNA was quantified by Nanodrop and reverse-transcribed into complementary DNA using SuperScript IV First-Strand Synthesis System (Invitrogen) in accordance with the manufacturer's instructions. The RT-qPCR reaction was performed in a Step One system using PCR SuperMix (ThermoFisher Scientific, #10572014). The delta-delta Ct method (2<sup>-ΔΔCt</sup>) was used to calculate the relative fold gene expression of samples using *Actb* as a control. Primer sequences are available in Supplementary Tables 3 and 4.

### RNA sequencing (RNA-seq)

Total RNA was extracted from cells using Qiagen RNeasy kit (#74004). RNA sequencing and data analysis was performed by the Beijing Genomics Institute. Briefly, 2 μg total RNAs were used for stranded RNA sequencing library preparation. Library was validated on the Agilent Technologies 2100 bioanalyzer. This project used the filtering software SOAPnuke developed by BGI independently for filtering. *P* value of GO analysis and KEGG enrichment analysis was calculated by using the basis function phyper of R. Then The *P* value was then corrected by multiple testing, and the corrected package was *q* value. *Q* value (corrected *P* value) ≤ 0.05 was used as the threshold.

### TCGA analysis

The analysis of The Cancer Genome Atlas (TCGA) dataset for PDAC and HGSOc was performed using the cBioPortal for Cancer Genomics, based on the Pan-Cancer Atlas run of the TCGA.

### Tumor Immune Dysfunction and Exclusion (TIDE) analysis

The association between TP53BP1 and Shieldin components (*PTIP*, *RIF1*, *RNF168*, *REV7*, *SHLD1*, and *SHLD2*) expression and cytotoxic T lymphocyte (CTL) infiltration level was estimated as the average expression level of *CD8A*, *CD8B*, *GZMA*, *GZMB* and *PRF* and with overall survival of patients with metastatic urothelial cancer treated with anti-PD-L1 agent (atezolizumab)<sup>65</sup>. The association between gene expression and CTL level was tested using Pearson correlation and the association between gene expression and patient survival was tested by the two-sided Wald test in a Cox-PH regression as implemented in TIDE computational framework<sup>78</sup>.

### siRNA transfection

For siRNA transfection, cells were seeded at 1 × 10<sup>5</sup> cells/mL into 6-well plates one day prior to planned transfection. Specific siRNA duplexes targeting *Mre11* (sc-37396), *Exo1* (sc-44880), or *TP53BP1* (sc-37455) were transfected using Lipofectamine RNAiMAX Reagent (Life Technologies) according to the manufacturer's protocol.

### Statistical analysis

Statistical analysis was performed using Prism software (GraphPad Prism 9.0 software). Data are presented as the mean ± standard error of the mean (in vivo) or mean ± standard deviation (in vitro). For comparisons of 2 groups, a two-tailed unpaired t-test was performed. For comparisons of 3 or more groups, one-way ANOVA was performed.

### Reporting summary

Further information on research design is available in the Nature Portfolio Reporting Summary linked to this article.

### Data availability

The RNA-seq data generated in this study have been deposited in the GEO database under accession code [GSE237615](https://www.ncbi.nlm.nih.gov/geo/query/acc.cgi?acc=GSE237615). RNA-seq data based on the pan-Cancer Atlas run of the TCGA were obtained from the cBioPortal (<https://www.cbioportal.org/>). The data used for testing association between gene expression and CTL level are available in TISIDB database (<http://cis.hku.hk/TISIDB/index.php>). The remaining data are available within the Article, Supplementary Information or Source Data file. Source data are provided as a Source Data file. Source data are provided with this paper.

### References

1. Sung, P. & Klein, H. Mechanism of homologous recombination: mediators and helicases take on regulatory functions. *Nat. Rev. Mol. Cell Biol.* **7**, 739–750 (2006).
2. Heyer, W. D., Ehmsen, K. T. & Liu, J. Regulation of homologous recombination in eukaryotes. *Annu Rev. Genet.* **44**, 113–139 (2010).

3. Chapman, J. R., Taylor, M. R. & Boulton, S. J. Playing the end game: DNA double-strand break repair pathway choice. *Mol. Cell* **47**, 497–510 (2012).
4. Bunting, S. F. & Nussenzweig, A. End-joining, translocations and cancer. *Nat. Rev. Cancer* **13**, 443–454 (2013).
5. Helleday, T., Eshtad, S. & Nik-Zainal, S. Mechanisms underlying mutational signatures in human cancers. *Nat. Rev. Genet.* **15**, 585–598 (2014).
6. Carvalho, C. M. & Lupski, J. R. Mechanisms underlying structural variant formation in genomic disorders. *Nat. Rev. Genet.* **17**, 224–238 (2016).
7. Reina-San-Martin, B., Chen, J., Nussenzweig, A. & Nussenzweig, M. C. Enhanced intra-switch region recombination during immunoglobulin class switch recombination in 53BP1<sup>-/-</sup> B cells. *Eur. J. Immunol.* **37**, 235–239 (2007).
8. Bothmer, A. et al. 53BP1 regulates DNA resection and the choice between classical and alternative end joining during class switch recombination. *J. Exp. Med.* **207**, 855–865 (2010).
9. Noordermeer, S. M. et al. The shieldin complex mediates 53BP1-dependent DNA repair. *Nature* **560**, 117–121 (2018).
10. Dimitrova, N., Chen, Y. C., Spector, D. L. & de Lange, T. 53BP1 promotes non-homologous end joining of telomeres by increasing chromatin mobility. *Nature* **456**, 524–528 (2008).
11. Lottersberger, F., Bothmer, A., Robbiani, D. F., Nussenzweig, M. C. & de Lange, T. Role of 53BP1 oligomerization in regulating double-strand break repair. *Proc. Natl Acad. Sci. USA* **110**, 2146–2151 (2013).
12. Sfeir, A. & de Lange, T. Removal of shelterin reveals the telomere end-protection problem. *Science* **336**, 593–597 (2012).
13. Lo, K. W. et al. The 8-kDa dynein light chain binds to p53-binding protein 1 and mediates DNA damage-induced p53 nuclear accumulation. *J. Biol. Chem.* **280**, 8172–8179 (2005).
14. He, Y. J. et al. DYNLL1 binds to MRE11 to limit DNA end resection in BRCA1-deficient cells. *Nature* **563**, 522–526 (2018).
15. Swift, M. L. et al. Dynamics of the DYNLL1-MRE11 complex regulate DNA end resection and recruitment of Shieldin to DSBs. *Nat. Struct. Mol. Biol.* **30**, 1456–1467 (2023).
16. Chapman, J. R. et al. RIF1 is essential for 53BP1-dependent non-homologous end joining and suppression of DNA double-strand break resection. *Mol. Cell* **49**, 858–871 (2013).
17. Daley, J. M. & Sung, P. RIF1 in DNA break repair pathway choice. *Mol. Cell* **49**, 840–841 (2013).
18. Di Virgilio, M. et al. Rif1 prevents resection of DNA breaks and promotes immunoglobulin class switching. *Science* **339**, 711–715 (2013).
19. Escribano-Diaz, C. et al. A cell cycle-dependent regulatory circuit composed of 53BP1-RIF1 and BRCA1-CtIP controls DNA repair pathway choice. *Mol. Cell* **49**, 872–883 (2013).
20. Feng, L., Fong, K. W., Wang, J., Wang, W. & Chen, J. RIF1 counteracts BRCA1-mediated end resection during DNA repair. *J. Biol. Chem.* **288**, 11135–11143 (2013).
21. Munoz, I. M., Jowsey, P. A., Toth, R. & Rouse, J. Phospho-epitope binding by the BRCT domains of hPTIP controls multiple aspects of the cellular response to DNA damage. *Nucleic Acids Res.* **35**, 5312–5322 (2007).
22. Wang, X., Takenaka, K. & Takeda, S. PTIP promotes DNA double-strand break repair through homologous recombination. *Genes Cells* **15**, 243–254 (2010).
23. Ashworth, A. & Lord, C. J. Synthetic lethal therapies for cancer: what's next after PARP inhibitors? *Nat. Rev. Clin. Oncol.* **15**, 564–576 (2018).
24. Bryant, H. E. et al. Specific killing of BRCA2-deficient tumours with inhibitors of poly(ADP-ribose) polymerase. *Nature* **434**, 913–917 (2005).
25. Farmer, H. et al. Targeting the DNA repair defect in BRCA mutant cells as a therapeutic strategy. *Nature* **434**, 917–921 (2005).
26. Curtin, N. & Bai, P. PARPs, PAR and NAD metabolism and their inhibitors in cancer. *Cancers* **12**, <https://doi.org/10.3390/cancers12123494> (2020).
27. Murai, J. et al. Trapping of PARP1 and PARP2 by Clinical PARP Inhibitors. *Cancer Res.* **72**, 5588–5599 (2012).
28. van Wietmarschen, N. & Nussenzweig, A. Mechanism for synthetic lethality in BRCA-deficient cancers: no longer lagging behind. *Mol. Cell* **71**, 877–878 (2018).
29. Cong, K. et al. Replication gaps are a key determinant of PARP inhibitor synthetic lethality with BRCA deficiency. *Mol. Cell* **81**, 3128–3144.e3127 (2021).
30. Dias, M. P., Moser, S. C., Ganesan, S. & Jonkers, J. Understanding and overcoming resistance to PARP inhibitors in cancer therapy. *Nat. Rev. Clin. Oncol.* **18**, 773–791 (2021).
31. Ding, L. et al. PARP inhibition elicits STING-dependent antitumor immunity in Brca1-deficient ovarian cancer. *Cell Rep.* **25**, 2972–2980.e2975 (2018).
32. Pantelidou, C. et al. PARP inhibitor efficacy depends on CD8(+) T-cell recruitment via intratumoral STING pathway activation in BRCA-Deficient models of triple-negative breast cancer. *Cancer Discov.* **9**, 722–737 (2019).
33. Pettitt, S. J. et al. Clinical BRCA1/2 reversion analysis identifies hotspot mutations and predicted neoantigens associated with therapy resistance. *Cancer Discov.* **10**, 1475–1488 (2020).
34. Boersma, V. et al. MAD2L2 controls DNA repair at telomeres and DNA breaks by inhibiting 5' end resection. *Nature* **521**, 537–540 (2015).
35. Bouwman, P. et al. 53BP1 loss rescues BRCA1 deficiency and is associated with triple-negative and BRCA-mutated breast cancers. *Nat. Struct. Mol. Biol.* **17**, 688–695 (2010).
36. Bunting, S. F. et al. 53BP1 inhibits homologous recombination in Brca1-deficient cells by blocking resection of DNA breaks. *Cell* **141**, 243–254 (2010).
37. Dev, H. et al. Shieldin complex promotes DNA end-joining and counters homologous recombination in BRCA1-null cells. *Nat. Cell Biol.* **20**, 954–965 (2018).
38. Barazas, M. et al. The CST complex mediates end protection at double-strand breaks and promotes PARP inhibitor sensitivity in BRCA1-deficient cells. *Cell Rep.* **23**, 2107–2118 (2018).
39. Xu, G. et al. REV7 counteracts DNA double-strand break resection and affects PARP inhibition. *Nature* **521**, 541–544 (2015).
40. Schultz, L. B., Chehab, N. H., Malikzay, A. & Halazonetis, T. D. p53 binding protein 1 (53BP1) is an early participant in the cellular response to DNA double-strand breaks. *J. Cell Biol.* **151**, 1381–1390 (2000).
41. Ward, I. M., Minn, K., van Deursen, J. & Chen, J. p53 Binding protein 53BP1 is required for DNA damage responses and tumor suppression in mice. *Mol. Cell Biol.* **23**, 2556–2563 (2003).
42. Konstantinopoulos, P. A., Ceccaldi, R., Shapiro, G. I., & D'Andrea, A. D. Homologous recombination deficiency: exploiting the fundamental vulnerability of ovarian cancer. *Cancer Discov.* **5**, 1137–1154 (2015).
43. Golan, T. et al. Maintenance Olaparib for Germline BRCA-Mutated Metastatic Pancreatic Cancer. *N. Engl. J. Med.* **381**, 317–327 (2019).
44. Hopkins, J. L., Lan, L. & Zou, L. DNA repair defects in cancer and therapeutic opportunities. *Genes Dev.* **36**, 278–293 (2022).
45. Germano, G. et al. Inactivation of DNA repair triggers neoantigen generation and impairs tumour growth. *Nature* **552**, 116–120 (2017).
46. Mandal, R. et al. Genetic diversity of tumors with mismatch repair deficiency influences anti-PD-1 immunotherapy response. *Science* **364**, 485–491 (2019).
47. Raskov, H., Orhan, A., Salanti, A., Gaggari, S. & Gogenur, I. Natural killer cells in cancer and cancer immunotherapy. *Cancer Lett.* **520**, 233–242 (2021).

48. Ru, B. et al. TISIDB: an integrated repository portal for tumor-immune system interactions. *Bioinformatics* **35**, 4200–4202 (2019).
49. Callen, E. et al. 53BP1 mediates productive and mutagenic DNA repair through distinct phosphoprotein interactions. *Cell* **153**, 1266–1280 (2013).
50. Zimmermann, M., Lotterberger, F., Buonomo, S. B., Sfeir, A. & de Lange, T. 53BP1 regulates DSB repair using Rif1 to control 5' end resection. *Science* **339**, 700–704 (2013).
51. Gao, S. et al. An OB-fold complex controls the repair pathways for DNA double-strand breaks. *Nat. Commun.* **9**, 3925 (2018).
52. Gupta, R. et al. DNA repair network analysis reveals Shieldin as a key regulator of NHEJ and PARP inhibitor sensitivity. *Cell* **173**, 972–988.e923 (2018).
53. Mirman, Z. et al. 53BP1-RIF1-shieldin counteracts DSB resection through CST- and Polalpha-dependent fill-in. *Nature* **560**, 112–116 (2018).
54. Setiawati, D. & Durocher, D. Shieldin - the protector of DNA ends. *EMBO Rep.* **20**, <https://doi.org/10.15252/embr.201847560> (2019).
55. Pennington, K. P. et al. 53BP1 expression in sporadic and inherited ovarian carcinoma: Relationship to genetic status and clinical outcomes. *Gynecol. Oncol.* **128**, 493–499 (2013).
56. Roby, K. F. et al. Development of a syngeneic mouse model for events related to ovarian cancer. *Carcinogenesis* **21**, 585–591 (2000).
57. Li, J. et al. Tumor cell-intrinsic factors underlie heterogeneity of immune cell infiltration and response to immunotherapy. *Immunity* **49**, 178–193.e177 (2018).
58. Kanehisa, M., Goto, S., Sato, Y., Furumichi, M. & Tanabe, M. KEGG for integration and interpretation of large-scale molecular data sets. *Nucleic Acids Res.* **40**, D109–D114 (2012).
59. Parker, B. S., Rautela, J. & Hertzog, P. J. Antitumor actions of interferons: implications for cancer therapy. *Nat. Rev. Cancer* **16**, 131–144 (2016).
60. Tietze, J. K. et al. Delineation of antigen-specific and antigen-nonspecific CD8(+) memory T-cell responses after cytokine-based cancer immunotherapy. *Blood* **119**, 3073–3083 (2012).
61. De Benedetti, F., Prencipe, G., Bracaglia, C., Marasco, E. & Grom, A. A. Targeting interferon-gamma in hyperinflammation: opportunities and challenges. *Nat. Rev. Rheumatol.* **17**, 678–691 (2021).
62. Liu, J., Geng, X., Hou, J. & Wu, G. New insights into M1/M2 macrophages: key modulators in cancer progression. *Cancer Cell Int.* **21**, 389 (2021).
63. Garcia-Diaz, A. et al. Interferon receptor signaling pathways regulating PD-L1 and PD-L2 expression. *Cell Rep.* **19**, 1189–1201 (2017).
64. Drane, P. et al. TIRR regulates 53BP1 by masking its histone methyl-lysine binding function. *Nature* **543**, 211–216 (2017).
65. Mariathasan, S. et al. TGFbeta attenuates tumour response to PD-L1 blockade by contributing to exclusion of T cells. *Nature* **554**, 544–548 (2018).
66. Cristescu, R. et al. Pan-tumor genomic biomarkers for PD-1 checkpoint blockade-based immunotherapy. *Science* **362**, <https://doi.org/10.1126/science.aar3593> (2018).
67. Kim, K., Jeon, S., Kim, T. M. & Jung, C. K. Immune gene signature delineates a subclass of papillary thyroid cancer with unfavorable clinical outcomes. *Cancers* **10**, <https://doi.org/10.3390/cancers10120494> (2018).
68. Le, D. T. et al. Mismatch repair deficiency predicts response of solid tumors to PD-1 blockade. *Science* **357**, 409–413 (2017).
69. Goodman, A. M. et al. Tumor mutational burden as an independent predictor of response to immunotherapy in diverse cancers. *Mol. Cancer Ther.* **16**, 2598–2608 (2017).
70. Guan, J. et al. MLH1 deficiency-triggered DNA hyperexcision by exonuclease 1 activates the cGAS-STING pathway. *Cancer Cell* **39**, 109–121.e105 (2021).
71. Gekara, N. O. DNA damage-induced immune response: Micronuclei provide key platform. *J. Cell Biol.* **216**, 2999–3001 (2017).
72. Sen, T. et al. Targeting DNA damage response promotes antitumor immunity through STING-mediated T-cell activation in small cell lung cancer. *Cancer Discov.* **9**, 646–661 (2019).
73. Ablasser, A. et al. cGAS produces a 2'-5'-linked cyclic dinucleotide second messenger that activates STING. *Nature* **498**, 380–384 (2013).
74. Dunphy, G. et al. Non-canonical activation of the DNA Sensing Adaptor STING by ATM and IFI16 mediates NF-kappaB signaling after nuclear DNA damage. *Mol. Cell* **71**, 745–760.e745 (2018).
75. Zhao, F., Kim, W., Kloeber, J. A. & Lou, Z. DNA end resection and its role in DNA replication and DSB repair choice in mammalian cells. *Exp. Mol. Med.* **52**, 1705–1714 (2020).
76. Bhin, J. et al. Multi-omics analysis reveals distinct non-reversion mechanisms of PARPi resistance in BRCA1- versus BRCA2-deficient mammary tumors. *Cell Rep.* **42**, 112538 (2023).
77. Yap, T. A. et al. Avelumab Plus Talazoparib in patients with advanced solid tumors: the JAVELIN PARP medley nonrandomized controlled trial. *JAMA Oncol.* **9**, 40–50 (2023).
78. Fu, J. et al. Large-scale public data reuse to model immunotherapy response and resistance. *Genome Med.* **12**, 21 (2020).

## Acknowledgements

D.C. and the research were supported by R01 CA208244 and R01 CA264900, Gray Foundation Team Science Award, DOD Ovarian Cancer Award W81XWH-15-0564/OC140632, Tina's Wish Foundation, V Foundation Award, BPGbio, and the Claudia Adams Barr Program in Innovative Basic Cancer Research. J.P.-F. is funded by the AGA Research Foundation's Research Scholar Award (AGA2023-13-03) and by a David Livingston Early Career Investigator Award. We thank Dana-Farber Cancer Institute for use of the Flow Cytometry Core, which provided flow cytometry services. DF/HCC is supported in part by NCI Cancer Center Support Grant NIH P30 CA 006516.

## Author contributions

Y.S., J.P.-F., A.S., W.F., P.A.K., and D.C. designed experiments. Y.S., J.P.-F., S.H., Z.L., Z.N., Y.H., S.K., and Y.J.K. performed experiments and contributed to data acquisition. Y.S., J.P.-F., Z.N., W.F., P.A.K., and D.C. analyzed and interpreted data. J.P.-F., P.A.K., and D.C. drafted the manuscript with input from all the authors. All authors read and agreed on the final version of the submitted manuscript and are accountable for all aspects of the work.

## Competing interests

The authors declare no competing interests.

## Additional information

**Supplementary information** The online version contains supplementary material available at <https://doi.org/10.1038/s41467-024-50999-2>.

**Correspondence** and requests for materials should be addressed to Dipanjan Chowdhury.

**Peer review information** *Nature Communications* thanks the anonymous reviewer(s) for their contribution to the peer review of this work. A peer review file is available.

**Reprints and permissions information** is available at <http://www.nature.com/reprints>

**Publisher's note** Springer Nature remains neutral with regard to jurisdictional claims in published maps and institutional affiliations.

**Open Access** This article is licensed under a Creative Commons Attribution-NonCommercial-NoDerivatives 4.0 International License, which permits any non-commercial use, sharing, distribution and reproduction in any medium or format, as long as you give appropriate credit to the original author(s) and the source, provide a link to the Creative Commons licence, and indicate if you modified the licensed material. You do not have permission under this licence to share adapted material derived from this article or parts of it. The images or other third party material in this article are included in the article's Creative Commons licence, unless indicated otherwise in a credit line to the material. If material is not included in the article's Creative Commons licence and your intended use is not permitted by statutory regulation or exceeds the permitted use, you will need to obtain permission directly from the copyright holder. To view a copy of this licence, visit <http://creativecommons.org/licenses/by-nc-nd/4.0/>.

© The Author(s) 2024